Computational modelling of compressible nonisothermal viscoelastic fluids

A.T. Mackay, T.N. Phillips *

School of Mathematics, Cardiff University, Abacws, Cardiff CF24 4AG, UK

ARTICLE INFO

ABSTRACT

The prediction of compressible nonisothermal flows of viscoelastic fluids is important in many industrial processes. Until relatively recently, there was a lack of tractable thermodynamically consistent mathematical models for this class of flows. In this paper a stabilised finite element scheme is presented for the models developed by the authors Mackay and Phillips (2019) which incorporates compressibility and nonisothermal effects. Numerical results are presented for variants of a couple of benchmark problems: the lid driven cavity and the natural convection problems. The temporal discretisation is based on the Taylor–Galerkin method. A compressible version of the discrete elastic viscous split stress (DEVSS) formulation is used to stabilise the numerical scheme. The combined and separate influence of compressible, viscoelastic and thermal effects on the characteristics of these benchmark flows is studied for the first time.

1. Introduction

Viscoelastic flows are present in a wide range of modern day industrial applications of complex fluids such as oil recovery, drug delivery, ink-jet printing, injection moulding and polymer processing. Physical experiments are often costly and impractical and therefore theoretical and computational analysis of viscoelastic flow is a vital tool in the improvement of these industrial processes. The inherent sophistication of mathematical models for viscoelastic fluids, such as Oldroyd-B, Giesekus, PTT, and FENE-P, mean that numerical methods are required to obtain solutions to viscoelastic flow problems. Even in simple geometries viscoelastic flows exhibit complex behaviour including shear-thinning, extensional-hardening, transient flow patterns and complex secondary flows [1]. Numerical simulations are an inexpensive alternative to physical experiments and enable flow predictions to be made that would otherwise be impossible to obtain. Since the 1970s improvements have been made to both the accuracy and computational efficiency of numerical simulations of polymeric fluids. The main contributing factor to this improvement has been an increase in computer processing power. However, several hurdles in both modelling and numerical analysis have also been overcome.

A large proportion of the literature on non-Newtonian flow is limited to incompressible and isothermal problems. Well-known predictor–corrector schemes such as Chorin's projection method rely on the divergence-free velocity field condition in order to update the velocity at each time step. However enforcing the incompressibility condition results in the pressure becoming a Lagrange multiplier and therefore any thermodynamic information about the pressure is lost [2]. In industrial polymer processing operations, such as injection moulding and high-speed extrusion, pressure, flow rate and temperature variation may be large. Hence, compressibility effects within the viscoelastic regime may become important and influence resulting flow behaviour and phenomena. The difference between incompressible and compressible flows is determined by the propagation speed of longitudinal waves, c, which couples density with pressure via an equation of state. For incompressible fluids the speed of sound is infinite whereas for compressible fluids the speed is finite. In recent years there have been some development of numerical schemes for compressible flow. Keshtiban and Webster [3] developed a Taylor–Galerkin scheme and used it to successfully obtain solutions to several benchmark problems for viscoelastic flow. Numerical investigations of fluid transport problems involve finding solutions to coupled systems of equations governing momentum, density, pressure and extra-stress (state variables). In the case of Newtonian flow, the extra-stress can be expressed as a linear function of the rate of strain tensor. For viscoelastic flow the extra-stress tensor satisfies its own governing equation (constitutive law) and cannot be eliminated by direct substitution. Furthermore, if the fluid is assumed to be incompressible the density is constant and can be parametrised. In the more general case fluid density is governed by the conservation of mass equation and an equation of state. Detailed theoretical analysis of the laws governing compressible & nonisothermal viscoelastic fluid transport have been undertaken by Beris and Edwards [4,5] and Bollada and Phillips [2].

A major difficulty for all numerical simulations of viscoelastic flow is the so-called high Weissenberg number problem (HWNP), which

---

describes the failure of numerical schemes to reach mesh converged solutions to even simple flow problems beyond some critical value of the Weissenberg number. Consistent viscoelastic models capturing time dependent relaxation effects use objective derivatives in the constitutive equations, such as the upper convected derivative. At high Weissenberg numbers, the presence of deformation terms in these derivatives result in steep exponential profiles that are not well captured by polynomial interpolation functions. Errors resulting from the failure to properly balance deformation with convection leads to convergence failure for most numerical solution schemes unless further stabilisation techniques are employed.

A commonly used technique for overcoming the HWNP is the Streamline Upwind Petrov Galerkin (SUPG) method of Brooks and Hughes [6]. SUPG was first implemented to stabilise Oldroyd-B flow calculations by Marchal and Crochet [7]. A similar technique was used by Guénette and Fortin [8] for the analysis of PTT fluids. Another stabilisation widely used is Elastic Viscous Stress Splitting (EVSS), first proposed by Rajagopalan et al. [9]. EVSS was successful in stabilising finite element method solutions to flow between eccentrically rotating cylinders, a benchmark problem greatly affected by the high Weissenberg number problem due to sharp velocity gradients arising in the narrow gap. Subsequently a variety of similar methods have been developed such as Discrete Elastic Viscous Stress Splitting (DEVSS) [8], Explicitly Elliptic Momentum Equation (EEME) [9], DEVSS-G [10] and Discontinuous Galerkin (DG) methods [11]. A large number of studies concerning stabilised finite element methods for viscoelastic flow can be found. In most cases, finite element methods are stabilised by adding (artificial) mesh-dependent terms to the standard Galerkin approximation equation.

Fattal and Kupferman introduced the log-conformation representation (LCR) method, in which the constitutive equation is reformulated as an equation for the logarithm of the conformation matrix. Using log-conformation representation ensures the stress tensor remains symmetric positive during computations. Similar techniques have been proposed such as the square-root conformation tensor formulation (SRCR), proposed by Balci et al. [12], and the kernel conformation tensor formulation, proposed by Alfonso et al. [13]. The extension of the log-conformation formulation to constitutive equations for nonisothermal compressible viscoelastic fluids in which the material parameters are replaced by temperature dependent material functions has not been established and is a subject for future development.

In recent years further advancements have been made in overcoming the HWNP for finite element approximations of Oldroyd-B flow. Venkatesan and Ganesan [1] developed a three-field formulation based on one-level Local Projection Stabilisation (LPS) when investigating Oldroyd-B flow in a wide channel. Using enriched approximation spaces and control terms in order to stabilise the constitutive and momentum equations they were able to compute solutions to the benchmark problems of flow past a sphere and lid-driven cavity flow for a wide range of Reynolds and Weissenberg numbers.

The temporal scheme used in this paper employs a decoupled scheme based on a fractional step approach. Fractional step methods have the advantage of decomposing the problem into a number of subproblems that are easier to solve computationally since each subproblem is a fraction of the size of the fully coupled set of equations. Another advantage of this class of methods is that it facilitates the use of specialised solution methods which may be appropriate for each of the subproblems separately but not for fully coupled methods. In the context of viscoelastic flows, several fractional step methods have been proposed. One of the earliest contributions is that of Saramito [14] who generalised the θ-method to viscoelastic flow based on three steps: a generalised Stokes problem for velocity and pressure with a given stress field; a hyperbolic constitutive equation for the extra-stress; a second generalised Stokes problem which enhances the overall stability of the scheme.

More recently, Castillo and Codina [15] designed several fractional step methods using a stabilised finite element formulation that allows equal order interpolation for velocity, pressure and stress. The methods can be viewed as an inexact LU block factorisations of the original fully coupled discrete problem and are designed at the pure algebraic level. Pacheco and Castillo [16] developed and implemented a consistent splitting scheme for viscoelastic fluid flows. The novel contribution of this scheme was the derivation of a consistent pressure Poisson equation (PPE) with consistent boundary conditions (BCs) which circumvents the necessity for a treatment of the divergence-free constraint. However, mass is conserved at the continuous level.

In this paper we consider the flow of both an incompressible ($Ma = 0$) and compressible ($Ma > 0$) Oldroyd-B fluid for two flows: the lid-driven cavity problem and buoyancy driven natural convection. A temporal scheme based on second-order Taylor–Galerkin pressure-correction scheme first proposed by Keshtiban and Webster [17,18] is employed. At each discrete timestep the spatial problem is approximated with Galerkin finite elements. Numerical results for incompressible flow will be used to benchmark the Taylor–Galerkin finite element scheme. Compressible flow dynamics are then analysed over a range of Reynolds, Weissenberg and Mach numbers. Mach numbers in the range $0.001 \leq Ma \leq 0.1$ are considered. Computations are stabilised using DEVSS and orthogonal projection stabilisation with the traditional DEVSS formulation being adapted in order to account for the compressible terms in the strain-rate tensor. The numerical scheme is implemented on a single CPU desktop using for the coarse meshed approximation. Packages from the FEniCS/DOLFIN finite element library are used in order to build the meshes and spatially discretise the stabilised equations at each time-step.

Nonisothermal convection flows are notoriously difficult to model because of the complex coupling between the momentum and thermal fields. These types of problems are classified as either forced convection, where the flow is generated by some external pump or fan, or as natural convection, where the flow is a result of density gradients within the flow. Buoyancy-driven flows are categorised as either external (free convection) or internal (natural convection) [19]. Modern developments in the understanding of buoyancy driven flows came during the period just after the Second World War [19]. However, it took nearly two decades before a satisfactory description of the problem was formulated and accurate computational models started to appear in the literature.

The earliest work on natural convection in a completely enclosed geometry was performed by Sparrow et al. [20], who performed an investigation into 'foam-like' insulating materials consisting of gas-filled cells dispersed throughout a solid material. Heat transfer through gas layers in rectangular geometries composed of adiabatic horizontal walls was first investigated by Batchelor [21] and Ostrach [19]. It was shown that the flow regime within the cavity was dependent on the height to width ratio, L/D, and the Rayleigh number, Ra [21]. For low values of Ra the investigation concluded that conduction was the dominant mode of heat transfer. In the asymptotic limit, $L/D \to \infty$, conduction was found to be the sole means of heat transport.

The first comprehensive study into this class of flow problems was undertaken by Ostrach [22]. Ostrach [23] also commented that internal convection flow problems are more complex than external convection flows. The reason for this is that a boundary layer forms an enclosed region around the core of the flow. The core flow is dependent on the boundary layer and vice versa. At large Rayleigh numbers the interaction between the two results in the onset of turbulence [19].

With the development of sophisticated numerical methods and access to high-performance computing facilities, the simulation of flows in enclosed geometries such as the natural convection problem has become one of the benchmark problems in computational fluid dynamics. The vast majority of the literature consists of studies of Newtonian flow at Rayleigh numbers in the range $[10^3, 10^7]$, where the solutions

provide good predictions of low viscosity/large length scale buoyancy-driven flows. However, the literature on non-Newtonian convective heat flow problems is sparse with very few publications in the literature that consider the behaviour of viscoelastic fluids. An investigation into power law fluids by Kim et al. [24] found that for high values of the Rayleigh number and moderate values of the Prandtl number, the overall heat transfer was enhanced as the power-law index is decreased i.e. as the fluid became more shear-thinning. An experimental study by Pittman et al. [25] showed that the rheological properties of a fluid are a significant factor in determining its thermal convective properties.

This paper is organised as follows. Sections 2–5 present the governing equations, reformulation of the momentum equation including stabilisation techniques, and the spatial and temporal numerical scheme. In Section 6 the computational domain, spatial discretisation and numerical solutions to the lid-driven cavity problem are presented with the solutions benchmarked against results from the literature. Analysis and results of the double-glazing problem are presented in Section 7 with the formulation, discretisation and results organised in a similar way to Section 6. Finally a short summary is provided in Section 8.

2. Governing equations

The governing equations comprising the conservation of mass, momentum and energy are given by

$$\frac{\partial \rho}{\partial t} + \nabla \cdot (\rho \mathbf{u}) = 0$$

$$\rho \frac{D\mathbf{u}}{Dt} = -\nabla p + \mu_s \left(\nabla^2 \mathbf{u} + \frac{1}{3} \nabla (\nabla \cdot \mathbf{u}) \right) + \nabla \cdot \boldsymbol{\tau}_p + \mathbf{F} \tag{1}$$

$$\rho C_p \frac{D\theta}{Dt} = -\nabla \cdot \mathbf{q} + \mathbf{T} : \nabla \mathbf{u} - p \nabla \cdot \mathbf{u}$$

where ρ is the density, $\mathbf{u}$ is the velocity, p is the pressure, $\mathbf{T} = 2\mu_s \mathbf{D} + \boldsymbol{\tau}_p$ is the extra-stress tensor, $\boldsymbol{\tau}_p$ is the polymeric contribution to $\mathbf{T}$, θ is absolute temperature, $\mathbf{q} = -\kappa \nabla \theta$ is the heat flux vector and $\mathbf{F}$ is the applied force. The material parameters are μ_s, the solvent viscosity, C_p, the specific heat at constant pressure and κ, the heat conduction coefficient.

The conformation tensor $\mathbf{C}$ is related to $\boldsymbol{\tau}_p$ by

$$\boldsymbol{\tau}_p = \frac{\mu_p}{\lambda(\theta)}(\mathbf{C} - \mathbf{I}) \tag{2}$$

where $\mathbf{C}$ satisfies the constitutive equation

$$\mathbf{C} + \lambda(\theta)(\overset{\triangledown}{\mathbf{C}} + (\nabla \cdot \mathbf{u})\mathbf{C}) = \mathbf{I}, \tag{3}$$

$\mathbf{D}$ is the rate-of-deformation tensor, μ_p is the polymeric viscosity and $\lambda(\theta)$ is the temperature-dependent relaxation time.

Finally, an equation of state is required to relate pressure and density. Here we use the equation

$$\frac{\partial p}{\partial \rho} = c_0^2 \left(1 + \alpha_v \frac{(\theta - \theta_0)}{\theta_0} \right) \tag{4}$$

where c_0 is the speed of sound and θ_0 is a reference temperature. The parameter α_v is the coefficient of thermal expansion with $\alpha_v = 0$ corresponding to isothermal flow and $\alpha_v = 1$ to an ideal gas equation.

Let L and U denote characteristic length and velocity scales, respectively. Introducing the dimensionless variables

$$\mathbf{u}^* = \frac{\mathbf{u}}{U} \quad \mathbf{x}^* = \frac{\mathbf{x}}{L} \quad t^* = \frac{tU}{L}$$
$$\rho^* = \frac{\rho}{\rho_0}, \quad p^* = \frac{Lp}{\mu_0 U}, \quad \theta^* = \frac{\theta - \theta_0}{\theta_h - \theta_0} \quad \tau_p^* = \frac{L\tau_p}{\mu_0 U} \tag{5}$$

The system of Eqs. (1), (3), (4) can be written in the following non-dimensional form

$$\frac{\partial \rho}{\partial t} + \nabla \cdot (\rho \mathbf{u}) = 0$$

$$Re\rho \frac{D\mathbf{u}}{Dt} = -\nabla p + \left[\beta_v \left(\nabla^2 \mathbf{u} + \frac{1}{3} \nabla (\nabla \cdot \mathbf{u}) \right) + \nabla \cdot \boldsymbol{\tau}_p \right] + \mathbf{F}$$

$$\rho \frac{D\theta}{Dt} = Di \nabla \cdot \tilde{\mathbf{q}} + V_h \boldsymbol{\sigma} : \nabla \mathbf{u} \tag{6}$$

$$\mathbf{C} + We (\overset{\triangledown}{\mathbf{C}} + (\nabla \cdot \mathbf{u})\mathbf{C}) = \mathbf{I}$$

$$\frac{\partial \rho}{\partial p} = \frac{Ma^2}{Re(1 + \tilde{\alpha}_v \theta)}$$

where

$$\boldsymbol{\sigma} = -p\mathbf{I} + 2\beta_v \mathbf{D} + \boldsymbol{\tau}_p \tag{7}$$

is the Cauchy stress tensor and

$$\tilde{\alpha}_v = \left(\frac{\theta_h - \theta_0}{\theta_0} \right) \alpha_v.$$

The dimensionless groups are Re, the Reynolds number, We, the Weissenberg number, Ma, the Mach number, β_v, the viscosity ratio, Di, the diffusion number and V_h, the viscous heating number, defined by

$$Re = \frac{\rho_0 U L}{\mu_0}, \qquad We = \frac{\lambda_0 U}{L},$$
$$Ma = \frac{U}{c_0}, \qquad \beta_v = \frac{\mu_s}{\mu_0}, \tag{8}$$
$$Di = \frac{\kappa}{\rho_0 C_p U L}, \qquad V_h = \frac{U \mu_0}{\rho_0 C_p L (\theta_h - \theta_0)}.$$

For buoyancy driven flows in a cavity an alternative non-dimensionalisation is used in which the characteristic velocity scale is $U = \alpha/L$ where $\alpha = \kappa/(\rho_0 C_p)$ is the thermal diffusivity. This gives rise to additional dimensionless groups: the Rayleigh number, Ra, and the Prandtl number, Pr, defined by

$$Ra = \frac{L^3 g}{v\alpha}(\theta_h - \theta_c), \quad Pr = \frac{v}{\alpha}, \tag{9}$$

where $v = \mu_0/\rho$ is the kinematic viscosity and $\theta_h - \theta_c$ is the temperature difference across the cavity.

The dimensionless equations are solved over a 2D computational domain Ω subject to given initial and boundary conditions. The boundary of Ω is denoted Γ. We subdivide the square boundary into 4 parts representing the straight edges: $\Gamma = \Gamma_D \cup \Gamma_N$, $\Gamma_D \cap \Gamma_N = \emptyset$, where Dirichlet conditions are imposed on Γ_D and Neumann conditions are imposed on Γ_N. Similarly, for temperature boundary conditions, we write $\Gamma = \Gamma_D^\theta \cup \Gamma_N^\theta$, $\Gamma_D^\theta \cap \Gamma_N^\theta = \emptyset$, where Dirichlet conditions are imposed on Γ_D^θ and Neumann conditions are imposed on Γ_N^θ.

3. Reformulation of the momentum equation

The governing equations are rewritten in a mathematically equivalent form to improve the ellipticity of the momentum equation and to stabilise the corresponding numerical approximation. The success of schemes introducing additional ellipticity into the momentum equation arises from the explicit form of the viscous operator in the momentum equation, which results in solving an elliptic saddle point problem. For viscoelastic fluids this viscous term is scaled with the viscosity ratio, β_v. Since we are interested predominantly in flows with dominant viscoelastic effects, β_v is small, typically $\beta_v \approx 0.1$. In this case the elastic stress contribution can dominate the viscous term, which in turn can lead to numerical instability. Perera and Walters [26] introduced a change of variable for the flow of a second-order fluid which ensured the well-posedness of the corresponding discrete system of equations by increasing the ellipticity of the momentum equation. This approach was employed in the elastic viscous split stress (EVSS) formulation by

Mendolson et al. [27] also for flows of second-order fluids. Since the change of variables performed in EVSS-type methods may be impossible for some constitutive equations, Guénette and Fortin [8] proposed the discrete EVSS (DEVSS) formulation, in which a change of variables is not required and the viscous term in the momentum equation is introduced only in an approximate sense.

In the case of incompressible flow, the rate-of-deformation tensor $\mathbf{D} = (\nabla\mathbf{u} + \nabla\mathbf{u}^T)$ is introduced as an additional variable and the dimensionless momentum equation is expressed in the form

$$Re\frac{D\mathbf{u}}{Dt} + \nabla p + \gamma_u(\nabla^2\mathbf{u} - \nabla\cdot\mathbf{D}) + \beta_v\nabla^2\mathbf{u} - \nabla\cdot\boldsymbol{\tau}_p = 0, \tag{10}$$

where γ_u is the DEVSS stabilisation parameter. At the continuous level, it is clear that the term multiplied by γ_u is equal to zero because $\nabla\cdot\mathbf{D} = \nabla^2\mathbf{u}$. However, this is not the case for the corresponding discrete problem when the approximation space for $\mathbf{D}$ does not contain the gradient of the approximation space for velocity. As a result, in regions of high deformation rate where stress gradients are large the DEVSS term stabilises the numerical solution.

In the case of compressible flow, Mackay and Phillips [28] proposed the following extension to the DEVSS formulation (10) in which the momentum equation is now expressed in the form

$$Re\frac{D\mathbf{u}}{Dt} + \nabla p + \gamma_u\left(\nabla^2\mathbf{u} + \frac{1}{3}\nabla(\nabla\cdot\mathbf{u}) - \nabla\cdot\mathbf{D}\right) + \beta_v\left(\nabla^2\mathbf{u} + \frac{1}{3}\nabla(\nabla\cdot\mathbf{u})\right) - \nabla\cdot\boldsymbol{\tau}_p = 0, \tag{11}$$

where the expression for $\mathbf{D}$ is given by

$$\mathbf{D} = \left(\nabla\mathbf{u} + \nabla\mathbf{u}^T - \frac{2}{3}(\nabla\cdot\mathbf{u})\mathbf{I}\right). \tag{12}$$

In both cases $\boldsymbol{\tau}_p$ is determined by Eq. (2) where $\mathbf{C}$ is the solution of the dimensionless version of the constitutive equation Eq. (3).

Brown et al. [29] used the velocity gradient tensor, $\mathbf{G} = \nabla\mathbf{u}$, as an additional unknown, instead of using the rate of deformation tensor, $\mathbf{D}$. In this method, called the EVSS-G formulation, the additional unknown, $\mathbf{G}$, is computed by means of an L^2 projection of $\nabla\mathbf{u}$. In analogy to the EVSS-G method, the DEVSS-G method (Liu et al. [30]) uses a projection of the velocity gradient tensor instead of the rate of deformation tensor. In this formulation, the velocity gradient projection tensor is used in the constitutive equation as well as in the momentum equation. This is the approach adopted in this paper. The solution space for the velocity gradient tensor is chosen to be $[L^2(\Omega)]^{2\times2}$ in order to be consistent with the spaces for pressure and polymeric stress, which are chosen to be $L_0^2(\Omega)$ and $[L^2(\Omega)]_s^{2\times2}$, respectively.

3.1. Explicit stabilisation of constitutive stress using orthogonal projection

In recent years, projection-based stabilisation techniques have been considered as a computationally efficient means of treating the numerical instabilities caused by the high Weissenberg problem [1,31]. Consider the explicit Euler time discretisation of the general constitutive equation in Eq. (6)

$$\frac{We(\mathbf{C}^{n+1} - \mathbf{C}^n)}{\Delta t} = [\mathbf{I} - \mathbf{C} - We\mathbf{F}(\mathbf{u},\mathbf{C}) - \mathbf{g}_2(\mathbf{C},\nabla\mathbf{u})]^n \tag{13}$$

where $\mathbf{F}$ is given by

$$\mathbf{F}(\mathbf{u},\mathbf{C}) = \mathbf{u}\cdot\nabla\mathbf{C} - \mathbf{C}\nabla\mathbf{u} + \nabla\mathbf{u}^T\mathbf{C} + (\nabla\cdot\mathbf{u})\mathbf{C} \tag{14}$$

and $\mathbf{g}$ is model dependent. If we define $\mathcal{Z}$ as the suitable function space for $\mathbf{C}$, the weak formulation can than be written in terms of an inner product

$$\frac{We}{\Delta t}\langle\mathbf{C}^{n+1} - \mathbf{C}^n,\mathbf{R}\rangle = \langle[\mathbf{I} - \mathbf{C} - We\mathbf{F}(\mathbf{u},\mathbf{C})]^n - \mathbf{g}_2(\mathbf{C},\nabla\mathbf{u}),\mathbf{R}\rangle \quad \forall\mathbf{R}\in\mathcal{Z} \tag{15}$$

The discrete approximation of Eq. (15) can be written in the form

$$\frac{We}{\Delta t}\langle\mathbf{C}_k^{n+1} - \mathbf{C}_k^n,\mathbf{R}\rangle$$

$$= \langle[\mathbf{I} - \mathbf{C}_k - We\mathbf{F}(\mathbf{u}_k,\mathbf{C}_k) - \mathbf{g}_2(\mathbf{C}_k,\nabla\mathbf{u}_k)]^n,\mathbf{R}\rangle \quad \forall\mathbf{R}_k\in\mathcal{Z}_k \tag{16}$$

where $\mathbf{u}_k \approx \mathbf{u}$ on some element $k \in \mathcal{T}$ (see next section for details of the discrete solution spaces used). Local projection stabilisation for the discrete problem can be described as follows: Let P_k be the L^2 projection onto an appropriate finite element space for velocity, polymeric stress or pressure, neglecting boundary conditions. Let $P_k^\perp = I - P_k$ be the orthogonal projection, where I is the identity mapping, i.e.

$$P^\perp(\mathbf{u}_k) = \int_\Omega (\mathbf{u}_k - \hat{\mathbf{u}}_k)\cdot\mathbf{v}_k\,d\Omega \quad \forall\mathbf{v}_k\in\mathcal{V} \tag{17}$$

where $\hat{\mathbf{u}}_k$ is the L^2 projection of $\mathbf{u}$ onto a lower order function space (for further details on the fluctuation operator, $P^\perp(\cdot)$ see Castillo et al. [32] and Ganesan et al. [33]). To stabilise the computations of the conformation stress the numerical diffusion term is added to the right-hand side of Eq. (16)

$$\mathbf{S}_{\tau_p}(\mathbf{C},\mathbf{R}) = \sum_{k\in\mathcal{T}}^{N_P} h_k\langle c_1\kappa_k\nabla\mathbf{C},\nabla\mathbf{R}\rangle + \sum_{k\in\mathcal{T}}^{N_P} h_k\langle c_2\kappa_k\nabla\cdot\mathbf{C},\nabla\cdot\mathbf{R}\rangle \tag{18}$$

where κ_k is the scalar fluctuation operator defined by

$$\kappa_k^{n+1} = \left\|\left|P^\perp\left[\frac{We}{\Delta t}(\mathbf{C}_k^{n+1} - \mathbf{C}_k^n) + \mathbf{C}_k^n + We\mathbf{F}^n(\nabla\mathbf{u}_k,\mathbf{C}_k) - \mathbf{I}\right]\right|\right\| \tag{19}$$

and c_1, c_2 are user chosen parameters. It is clear that, in the elements where $\mathbf{C}_k^n$ satisfies the discretised form of the constitutive equation, $\kappa_k = 0$. Thus the stabilised formulation of the discrete problem Eq. (16) can be written

$$\frac{We}{\Delta t}\langle\mathbf{C}_k^{n+1} - \mathbf{C}_k^n,\mathbf{R}\rangle + \mathbf{S}_{\tau_p}^{n+1} = \langle[\mathbf{I} - \mathbf{C}_k - We\mathbf{F}(\mathbf{u}_k,\mathbf{C}_k)]^n,\mathbf{R}\rangle \quad \forall\mathbf{R}_k\in\mathcal{Z}_k \tag{20}$$

3.2. Choice of stabilisation parameters

Without the use of stabilisation techniques, the numerical algorithm failed to converge beyond $t = 2$. With the addition of Local Projection and DEVSS stabilisations, the range of flow parameters for which stable solutions could be achieved was extended. However, care had to be exercised about the magnitude of the stabilisation parameters used since if the values were chosen to be too large then there was a reduction in the quality of the approximations, and they were not physically meaningful. For example, if the values of the parameters c_1 and c_2 in Eq. (18) were increased further, converged approximations were obtained for $We > 5$ but these were not physical. There is a range of stabilisation parameters which enhances stability of the scheme without impacting on the quality of the numerical approximations. These considerations motivated the choice of parameters used in this paper.

In the lid-driven cavity problem, for example, both LPS and DEVSS stabilisation were necessary. Specifically, LPS extended the range of We for which converged solutions were obtained from $We = 0.1$ to $We = 2$. The use of the DEVSS reformulation was necessary for extending the range of Re and Ma over which converged approximations were obtained.

The stabilisation terms are largest in regions where the gradient of the components of the stress tensor components is large (see Section 6), but tend to zero as the mesh resolution increases. The challenge is to find values of c_1 and c_2 such that the finite element solution converges without the stabilisation terms negatively impacting on the accuracy of the discrete conformation stress in any region of the flow. We found the most suitable range to be $0.01 \leq c_1, c_2 \leq 0.1$. In both Sections 6 and 7 numerical solutions were generated using the parameter choice $c_1 = 0.05$ and $c_2 = 0.01$.

4. Spatial discretisation

Each of the steps in the semi-discrete problem (29) are written in a weak formulation with the following choices of function spaces for the velocity, pressure, stress and temperature

$$\mathcal{V} = \left\{ \mathbf{v} \in H^1(\Omega)^2 : \mathbf{v} = \mathbf{v}_D \text{ on } \Gamma_D, \nabla \mathbf{v} \cdot \mathbf{n} = \mathbf{0} \text{ on } \Gamma_N \right\}, \tag{21}$$

$$\mathcal{Q} = \left\{ q \in L^2(\Omega) \right\}, \tag{22}$$

$$\mathcal{Z} = \left\{ \mathbf{R} : \quad R_{ij} \in L^2(\Omega), \quad R_{ij} = R_{ji}, \ i, j = 1, 2 \right\}, \tag{23}$$

$$\mathcal{Q}^T = \left\{ \theta \in H^1(\Omega) : \theta = \theta_D \text{ on } \Gamma_D^\theta, \ \nabla \theta \cdot \mathbf{n} = 0 \text{ on } \Gamma_N^\theta \right\}. \tag{24}$$

The weak formulation of the semi-discrete problem (29) is discretised using the finite element method. The computational domain, Ω, is partitioned into triangular finite elements. On each element, each dependent variable is approximated using a low-order polynomial in which the unknowns are the coefficients of the basis functions. These are the degrees of freedom of the problem, which are typically approximations to the dependent variables at the nodes. A set of algebraic equations is then derived by choosing appropriate test functions and evaluating or approximating the integrals that appear in the weak formulation of Eq. (29). Essentially a test function is associated with each unknown in the problem.

We define conforming finite element spaces $\mathcal{V}_h \subset \mathcal{V}$, $\mathcal{Q}_h \subset \mathcal{Q}$, $\mathcal{Z}_h \subset \mathcal{Z}$ and $\mathcal{Q}_h^T \subset \mathcal{Q}^T$ in the usual manner

$$\mathcal{V}_h = \left\{ \mathbf{v}_h \in H^1(\Omega)^2 : \mathbf{v} = \mathbf{v}_J \text{ on } \Gamma_J, \quad \mathbf{v}_h = \mathbf{0} \text{ on } \Gamma_B \right\}, \tag{25}$$

$$\mathcal{Q}_h = \left\{ q_h \in L^2(\Omega) \right\}, \tag{26}$$

$$\mathcal{Z}_h = \left\{ \mathbf{R} : \quad R_{h,ij} \in L^2(\Omega), \quad R_{h,ij} = R_{h,ji}, \quad i, j = 1, 2 \right\}, \tag{27}$$

$$\mathcal{Q}_h^T = \left\{ \theta_h \in H^1(\Omega) : \theta = \theta_0 \text{ on } \Gamma_J \right\}. \tag{28}$$

This combination of discrete function spaces ensures that the Ladyzhenskaya–Babuška–Brezzi (LBB) or inf-sup condition is satisfied. In this paper we restrict ourselves to three types of compatible finite elements suitable for modelling viscoelastic flow; namely $P1$ piecewise linear continuous Lagrangian elements for pressure, density and temperature, $P2$ piecewise quadratic continuous elements for velocity and $P1$ linear discontinuous Lagrangian elements for stress. In the implementation of DEVSS-G stabilisation we make use of the space of discontinuous functions over Ω constructed using $P0$ elements for approximating the components of $\nabla \mathbf{u}$.

5. Time discretisation: Taylor-Galerkin method

A Taylor–Galerkin method is used to discretise the governing equations in time. Taylor–Galerkin methods were initially developed for solving convective transport problems for which the governing equations are hyperbolic [34]. The motivation for Taylor–Galerkin methods stems from the desire to derive high-order accurate time-stepping schemes which can be used in conjunction with spatial discretisation methods. A two-step Taylor–Galerkin algorithm for computing nonisothermal and (weakly) compressible viscoelastic flow is given by

Step 1a
$$\left(\frac{\rho^{n+\frac{1}{2}} - \rho^n}{\Delta t/2} \right) = -\mathbf{u}^n \cdot \nabla \rho^n - \rho^n (\nabla \cdot \mathbf{u}^n)$$

Step 1b
$$Re \left(\frac{\rho^{n+\frac{1}{2}} \mathbf{u}^{n+\frac{1}{2}} - \rho^n \mathbf{u}^n}{\Delta t/2} \right) = \beta_v \left(\nabla^2 \mathbf{u}^n + \frac{1}{3} \nabla (\nabla \cdot \mathbf{u}^n) \right)$$
$$- Re \mathbf{u}^n \cdot \nabla \mathbf{u}^n + \nabla \cdot \boldsymbol{\tau}_p^n - \nabla p^n$$

Step 1c
$$We \left(\frac{\mathbf{C}^{n+\frac{1}{2}} - \mathbf{C}^n}{\Delta t/2} \right)$$
$$= [\mathbf{I} - \mathbf{C} - We(\mathbf{u} \cdot \nabla \mathbf{C} - \mathbf{C} \nabla \mathbf{u} + \nabla \mathbf{u}^T \mathbf{C} + \nabla \cdot \mathbf{u} \mathbf{C}) - \mathbf{g}_2(\mathbf{C}, \mathbf{D})]^n$$

Step 1d
$$\rho^n \left(\frac{\theta^{n+\frac{1}{2}} - \theta^n}{\Delta t/2} \right) = Di \nabla^2 \theta^n - \rho^n \mathbf{u}^n \cdot \nabla \theta^n$$
$$+ V_h(\boldsymbol{\sigma}^n : \nabla \mathbf{u}^n - p^n \nabla \cdot \mathbf{u}^n)$$

Step 2
$$Re \rho^n \left(\frac{\mathbf{u}^* - \mathbf{u}^n}{\Delta t} \right) = \frac{1}{2} \beta_v \left(\nabla^2 \mathbf{u}^n + \frac{1}{3} \nabla (\nabla \cdot \mathbf{u}^n) \right)$$
$$- Re \mathbf{u}^{n+\frac{1}{2}} \cdot \nabla \mathbf{u}^{n+\frac{1}{2}} + \nabla \cdot \boldsymbol{\tau}_p^{n+\frac{1}{2}} - \nabla p^n$$

Step 3
$$\left(\frac{\rho^{n+1} - \rho^n}{\Delta t} \right) = -\mathbf{u}^{n+\frac{1}{2}} \cdot \nabla \rho^{n+\frac{1}{2}} - \rho^{n+\frac{1}{2}} (\nabla \cdot \mathbf{u}^{n+\frac{1}{2}})$$

Step 4
$$p^{n+1} - p^n = \frac{Re(1 + \tilde{\alpha} \theta^n)}{Ma^2} (\rho^{n+1} - \rho^n)$$

Step 5
$$Re \left(\frac{\rho^{n+1} \mathbf{u}^{n+1} - \rho^n \mathbf{u}^*}{\Delta t} \right) = -\frac{1}{2} \nabla (p^{n+1} - p^n)$$
$$+ \frac{1}{2} \beta_v \left(\nabla^2 \mathbf{u}^{n+1} + \frac{1}{3} \nabla (\nabla \cdot \mathbf{u}^{n+1}) \right)$$

Step 6
$$We \left(\frac{\mathbf{C}^{n+1} - \mathbf{C}^n}{\Delta t} \right) + \mathbf{C}^{n+1} = [\mathbf{I}$$
$$- We(\mathbf{u} \cdot \nabla \mathbf{C} - \mathbf{C} \cdot \nabla \mathbf{u} + \nabla \mathbf{u}^T \cdot \mathbf{C} + (\nabla \cdot \mathbf{u}) \mathbf{C})$$
$$- \mathbf{g}_2(\mathbf{C}, \mathbf{D})]^{n+\frac{1}{2}}$$

Step 7
$$\left(\frac{\rho^{n+1} \theta^{n+1} - \rho^n \theta^n}{\Delta t} \right) = Di \nabla^2 \theta^{n+1} - \rho^{n+\frac{1}{2}} \mathbf{u}^{n+\frac{1}{2}} \cdot \nabla \theta^{n+\frac{1}{2}}$$
$$+ V_h(\boldsymbol{\sigma}^{n+\frac{1}{2}} : \nabla \mathbf{u}^{n+\frac{1}{2}} - p^n \nabla \cdot \mathbf{u}^n)$$

$$\tag{29}$$

The scheme given by (29) represents a second-order (in time) discretisation for the system of equations for weakly compressible viscoelastic flow (Eq. (6)).

Step 1 represents an explicit discretisation of the continuity, momentum, constitutive and energy equations over a half time step. An intermediate velocity is computed in Step 2 and together with Step 5 these represent a second-order Crank–Nicolson discretisation of the momentum equation. Step 3 is a discretisation of the continuity equation using the mid-point rule. Step 4 is a discretisation of the equation of state in which the temporal derivative of density is replaced by the temporal derivative of pressure using the chain rule

$$\frac{\partial \rho}{\partial t} = \frac{Ma^2}{Re(1 + \tilde{\alpha}\theta)} \frac{\partial p}{\partial t}. \tag{30}$$

Steps 5, 6 and 7 represent discretisations of the momentum, constitutive and energy equations, respectively, in which the nonlinear terms are evaluated using the mid-point rule and the linear terms are treated implicitly.

6. Regularised lid-driven cavity problem

In this section we compute solutions to the regularised lid-driven cavity problem. The fluid is contained in a square cavity $\Omega = [0, 1] \times [0, 1]$, bounded by solid walls with the top boundary moving from left to right. The boundary of Ω is denoted by $\partial \Omega$ with $\partial \Omega = \partial \Omega_1 \cup \partial \Omega_2$ where $\partial \Omega_1$ represents the moving lid (top boundary), and $\partial \Omega_2$ the other three sides of the boundary on which no-slip boundary conditions are imposed.

To mitigate against the numerical challenges caused by the initial rapid changes in deformation near the upper two corners, the lid velocity is regularised such that $\nabla \mathbf{u}$ vanishes at $(0, 1)$ and $(1, 1)$. Accordingly we use the velocity profile proposed by Venkatesan and Ganesan [1]

$$u_x(x, 1, t) = 8[1 + \tanh(8(t - 0.5))] x^2 (1 - x)^2$$
$$u_y(x, 1, t) = 0, \quad 0 \le x \le 1, \quad t \ge 0. \tag{31}$$

The velocity is ramped so that $\mathbf{u} \approx (0, 0)$ when $t = 0$. We also impose that $\boldsymbol{\tau}^p(x, y, 0) = \mathbf{0}$. The average horizontal velocity component of the
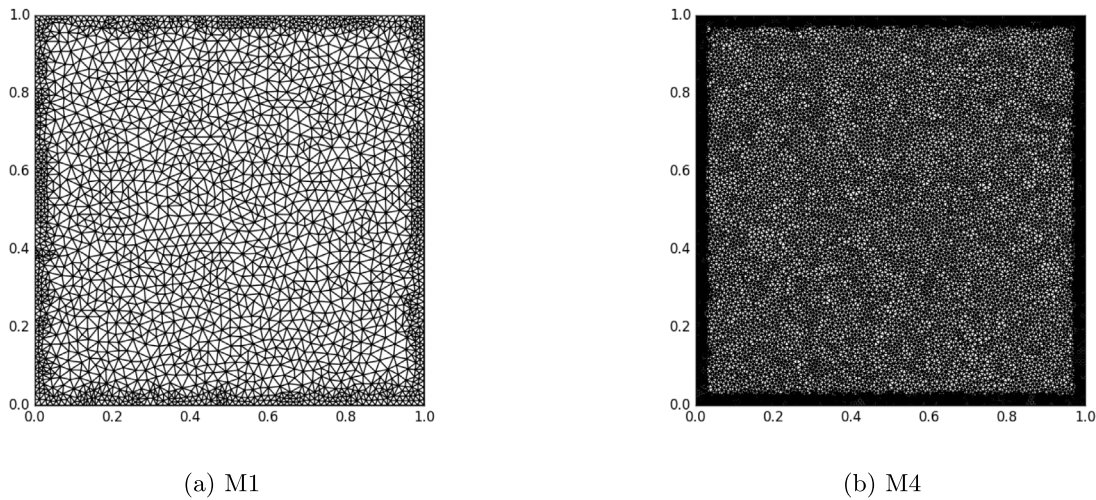
(a) M1

(b) M4

Fig. 1. Finite element meshes M1 and M4 for the lid driven cavity problem.

Table 1
Characteristics of the finite element meshes M1–M4 for the lid driven cavity problem.

Mesh	Cells	h_{min}	h_{max}	$DoF(p)$	$DoF(\mathbf{u})$	$DoF(C)$	Time/iteration
M1	3535	0.01109	0.03975	1854	14 484	21 726	0.94
M2	7813	0.00758	0.02651	4069	31 900	47 850	2.36
M3	13 889	0.00532	0.01989	7118	56 248	84 372	4.36
M4	31 024	0.00362	0.01326	15 836	125 390	188 085	7.24

Table 2
Lid-driven cavity problem: Convergence of the steady state values of (a) kinetic energy and (b) elastic energy values at $t = 15$ on meshes M1–M4 for $We = 0.5$, $Re = 0$.

Mesh	E_k	E_e	ψ_{min}	x_{min}	y_{min}
M1	0.0109	2.755	−0.0641	0.498	0.827
M2	0.0108	2.933	−0.0687	0.491	0.810
M3	0.0107	2.935	−0.0693	0.486	0.800
M4	0.0107	2.935	−0.0693	0.486	0.800

lid, $\hat{U}$, is given by

$$\hat{U} = \int_0^1 u_x(x,1,t)\,dx = \frac{4}{15}[1 + \tanh(8(t - 0.5))] \to \frac{8}{15} \qquad \text{as } t \to \infty \quad (32)$$

Sousa et al. [35] showed that the use of this regularisation of the lid velocity significantly reduces the strength of the main recirculation region compared with the unregularised problem. In order to better mimic the unregularised problem, weaker regularisations can be used in which the fluid moves at or close to the maximum velocity over a larger proportion of the top wall.

The domain, Ω is decomposed into triangular elements. Fig. 1 shows meshes M1 and M4 and Table 1 gives the mesh characteristics. The refinement method used is similar to the technique used by Venkastesan and Ganesan [1] where cells with centres within $0.05/L$ of the boundary are divided in two by connecting the mid-point of the longest side to the opposite vertex. The cell adjacent to the refined element is also subdivided in the same way to prevent the creation of a hanging node.

6.1. Results

All of the numerical simulations presented in this section (incompressible and compressible) utilise the DEVSS formulation with DEVSS parameter $\gamma_u = 1 - \beta_v$ and use orthogonal projection stabilisation with parameters $c_1 = 0.05$ and $c_2 = 0.01$. Results were generated on a four core single CPU machine and the numerical method was implemented using the FEniCS finite element library [36]. Python modules used to generate the following results can be found on the GitHub software repository [37]. Typical simulations had a run time of between 4-8 h depending on mesh resolution.

6.1.1. Mesh convergence

First we compare the kinetic and elastic energy profiles for the unstructured meshes in Fig. 1 in order to demonstrate the mesh convergence of the numerical approximation. Fig. 2 shows the evolution of the kinetic and potential energies for a compressible viscoelastic fluid defined by the parameters $Re = 10$, $We = 0.25$ and $Ma = 0.001$

on each of the four meshes M1–M4. The kinetic and elastic energies increase from 0 under the motion of the top wall with the kinetic energy responding faster than the elastic energy. The kinetic energy overshoots and attains its peak value at $t = 1$ before decreasing to its steady sate value at $t = 2$. The elastic energy increases monotonically and reaches its steady state value at $t = 4$. Convergence with mesh refinement is demonstrated. Apart from a small deviation in the kinetic energy during the transient period of the flow there is close agreement between the energy profiles throughout the duration of the simulation and especially at steady-state. Table 2 provides a convergence analysis of the steady state values of the kinetic and elastic energies for $We = 0.5$ and $Re = 0$. Also shown in this table is the minimum value of the stream function and its location. The values in this table demonstrate that convergence has been attained on M3.

In Fig. 3 we show the local influence of the various numerical stabilisation components of the numerical scheme for $Re = 0$, $We = 0.5$, $\beta_v = 0.5$ at $t = 2$. In Fig. 3(a) and (b), the contours of the relative errors in the normal components of the rate of deformation tensor $\mathbf{D}$ are shown. The maximum relative error is approximately 5×10^{-3} and as expected the dominant error is confined to a region near the top plate and is convected into the upper region of the cavity. Similarly, in Fig. 3(c) we present the contour plot of the scalar fluctuation parameter κ in the orthogonal projection scheme, where we have defined

$$\kappa = \left(\int_\Omega |\kappa_h|^2 d\Omega \right)^{1/2} \tag{33}$$

and κ_h is the orthogonal projection stabilisation term on element h defined in Eq. (19). This parameter is zero in the bulk of the domain and only becomes activated in elements near the top plate.

6.1.2. Incompressible flow

In this section comparisons are made between the predictions of the scheme proposed in this paper and results in the literature [1,35,38]. Contours of the velocity components are shown in Fig. 4. There is a significant build-up of viscoelastic stress in the region near the upper
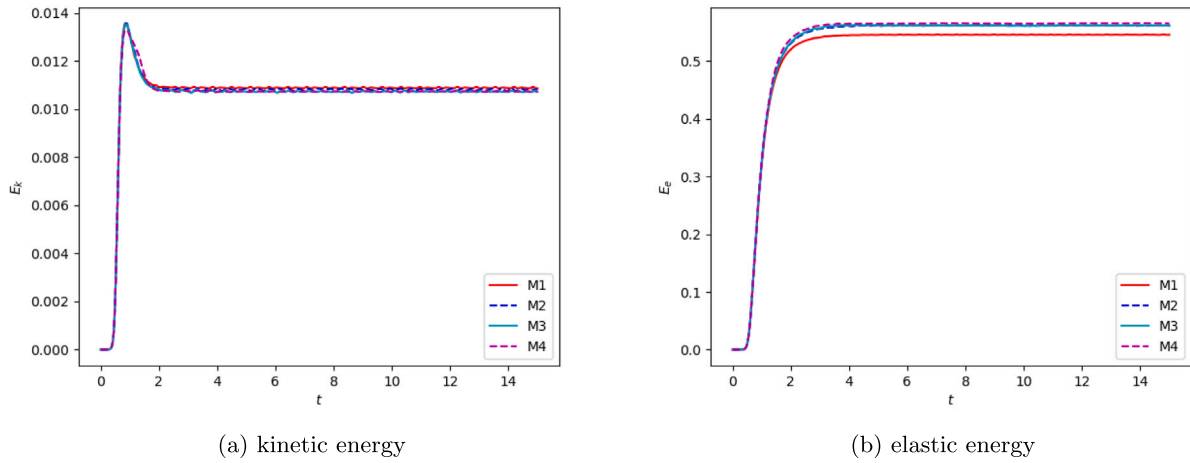
(a) kinetic energy   (b) elastic energy

Fig. 2. Lid-driven cavity problem: Influence of the evolution of (a) kinetic energy, (b) elastic energy for meshes M1–M4 for $We = 0.25$, $Re = 10.0$.
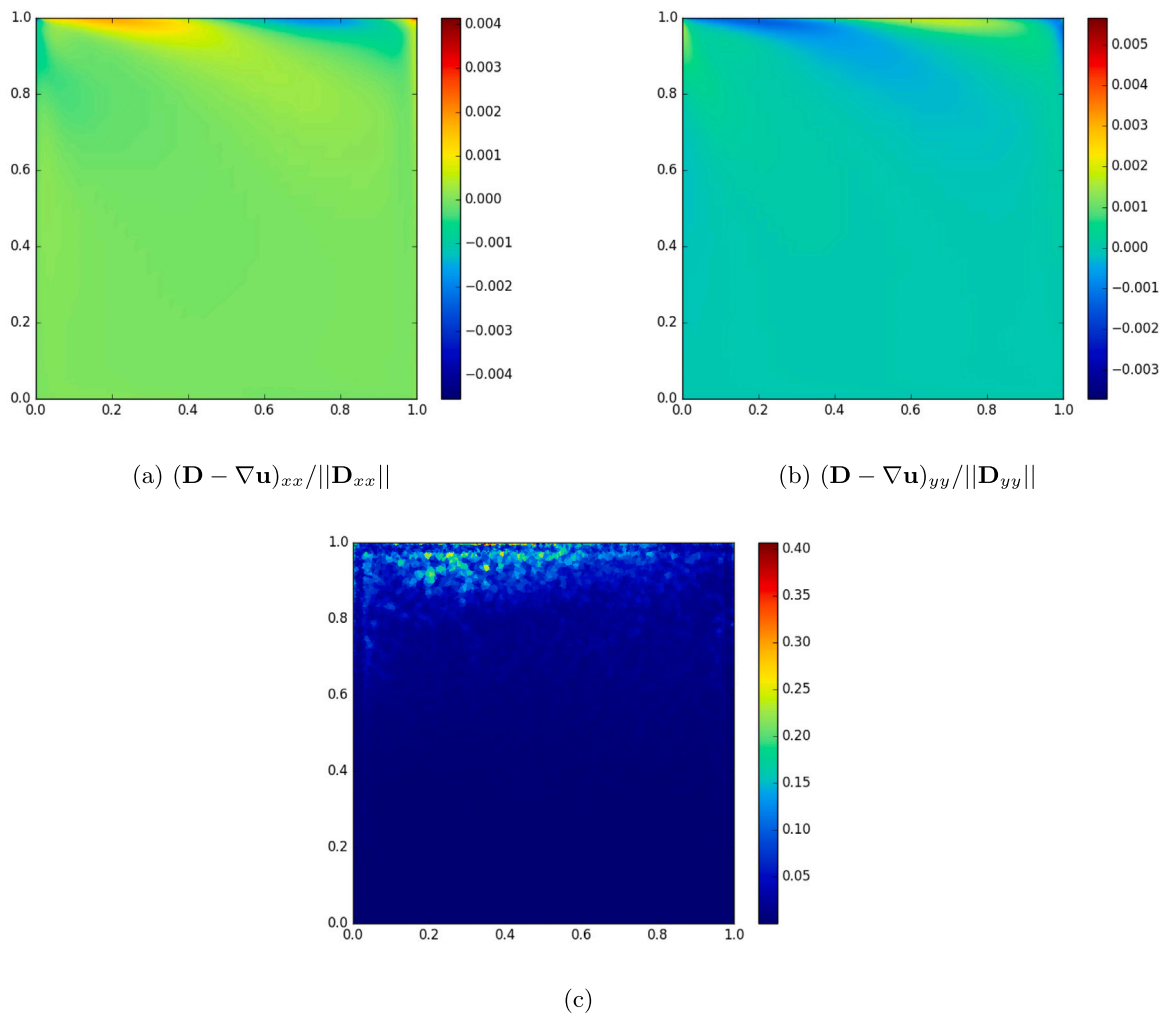

(a) $(\mathbf{D} - \nabla\mathbf{u})_{xx}/||\mathbf{D}_{xx}||$ (b) $(\mathbf{D} - \nabla\mathbf{u})_{yy}/||\mathbf{D}_{yy}||$

(c)

Fig. 3. Effect of numerical stabilisation for the lid driven cavity problem: Contours of the relative magnitude of the errors in the normal components of the velocity gradient tensor (a) $(\nabla\mathbf{u})_{xx}$, (b) $(\nabla\mathbf{u})_{yy}$ computed using DEVSS, (c) the scalar fluctuation parameter κ in the orthogonal projection scheme, at $t = 2.0$ ($Re = 0$, $We = 0.5$, $\beta_v = 0.5$).
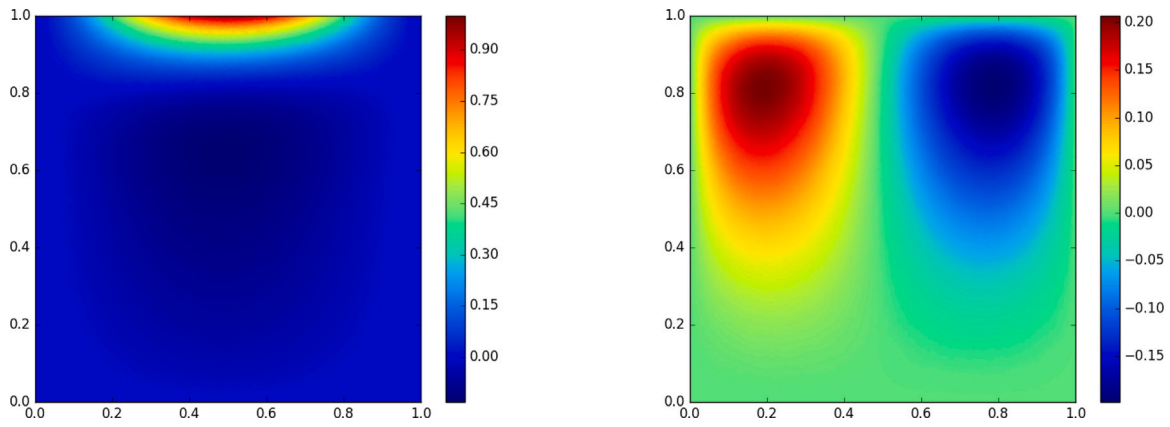
Fig. 4. Lid driven cavity flow: contours of the velocity components (a) u_x and (b) u_y for $We = 0.5$, $\beta_v = 0.5$, $Re = 0$ at $t = 10$.
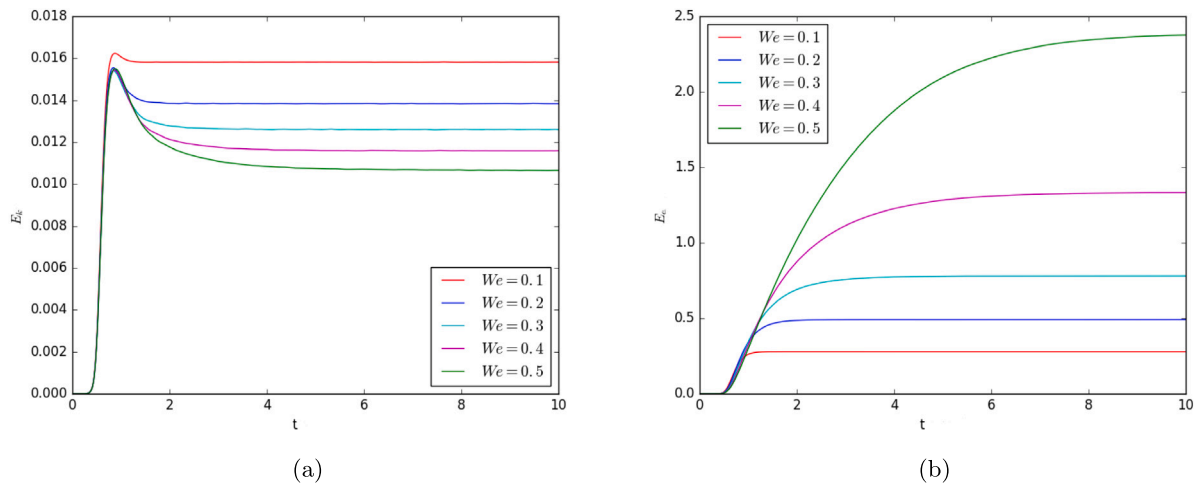

Fig. 5. Lid-driven cavity flow: (a) kinetic and (b) elastic energy for $We = 0.1, 0.2, 0.3, 0.4, 0.5$ and $Re = 1$ and $Ma = 0.01$.

Table 3
Incompressible lid driven cavity flow: Comparison of minimum value of stream function and its location with results in the literature for $We = 0.5$, $Re = 0$.

Reference	ψ_{min}	x_{min}	y_{min}
Current work	−0.0693	0.486	0.800
Venkatesan et al. [1]	−0.0698	0.470	0.798
Pan et al. [39]	−0.0700	0.469	0.798
Sousa et al. [35]	–	0.467	0.801
Castillo et al. [31]	–	0.470	0.800

right corner, pushing the eye of rotation to the left of its location for $We = 0$. Table 3 provides quantitative comparisons and shows that the predictions of the minimum value of the stream function and the y coordinate of its location are in good agreement with results in the literature [1,31,35,39]. Although the x coordinate of the location of the minimum value of the stream function has converged (see Table 2) it differs by 3% from other predictions in the literature. This may be due to the fact that the stream function is not a primary variable in this formulation which introduces interpolation error in the determination of the location of the minimum value of the stream function.

6.1.3. Compressible flow

In this section we present numerical results illustrating the effects of compressibility. Numerical simulations for compressible flow were generated for the following Mach numbers: $Ma = 0.001, 0.01, 0.1$. At these Mach numbers there is little qualitative difference in the behaviour of flow from the incompressible case. However, there are quantitative differences and we provide comparisons of the influence of Ma on kinetic and elastic energy, centre of recirculation and minimum value of the stream function.

Fig. 5 shows the influence of viscoelasticity on the evolution of the kinetic and potential elastic energy profiles for $Re = 1$ and $Ma = 0.01$. As anticipated the elastic energy is dominant over kinetic energy and the steady state value of the elastic energy increases monotonically and rapidly with respect to increases in the value of We. For $We = 0.5$ the elastic energy is more than two orders of magnitude greater than the kinetic energy. On the other hand there is a single overshoot in the kinetic energy for all values of We considered before it decreases to its steady state value. Velocity overshoots are a characteristic feature of viscoelastic flows with the magnitude of the overshoot increasing with increasing We [40]. This gives rise to the kinetic energy behaviour observed in Fig. 5 which exhibits similar overshoot behaviour. The steady state values of the kinetic energy decrease with respect to increases in the value of We and steady state values are reached by $t = 6$. The elastic energy takes longer to reach steady state and the tiem taken to reach steady state increases with increasing We.

Fig. 6 displays the same information for a larger value of Re. The evolution of the energy profiles in this figure are for $Re = 5$. The trends are the same as for Fig. 5 except that the influence of inertia has diminished the growth of the elastic energy with the steady state value of elastic energy reduced by around 25% for $We = 0.5$ while the corresponding steady state value of kinetic energy is increased by around 10%.
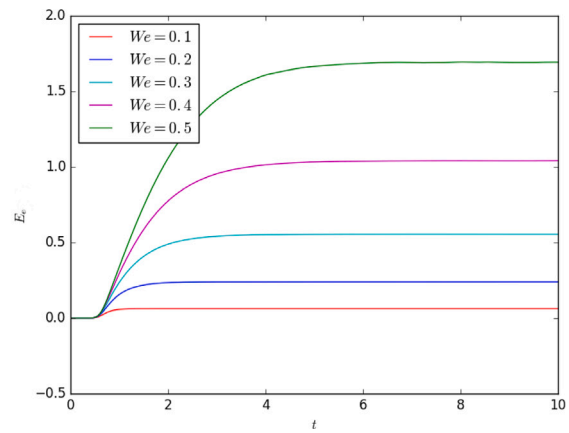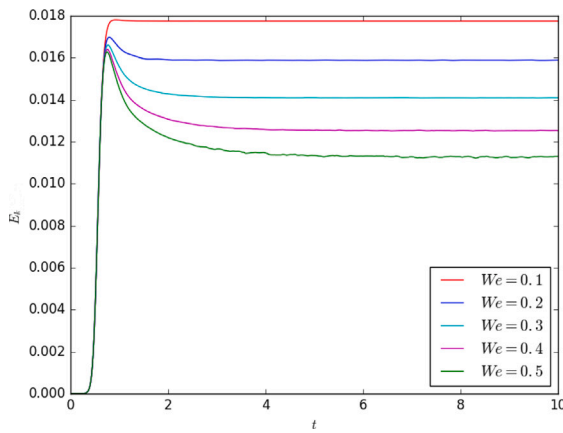
Fig. 6. Lid-driven cavity flow: (a) kinetic and (b) elastic energy for $We = 0.1, 0.2, 0.3, 0.4, 0.5$ and $Re = 5$ and $Ma = 0.01$.
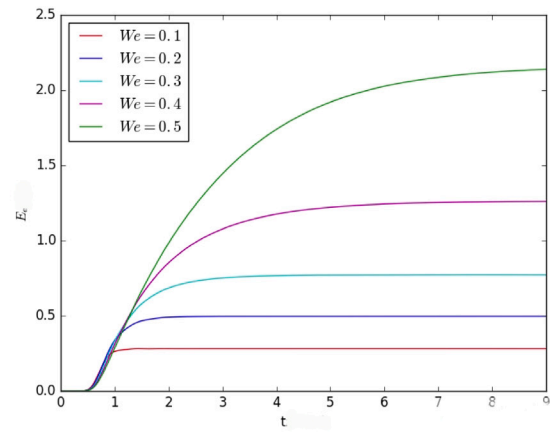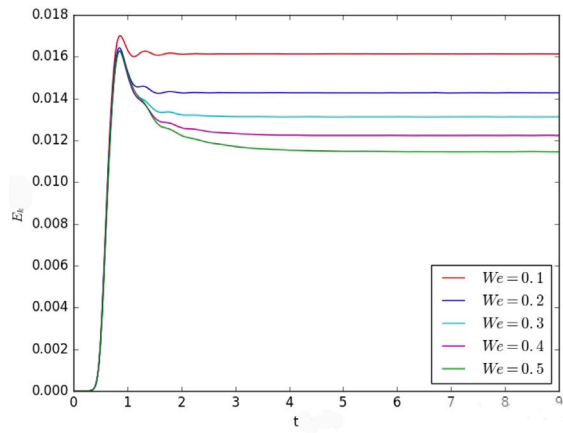

Fig. 7. Lid-driven cavity flow: (a) kinetic and (b) elastic energy for $We = 0.1, 0.2, 0.3, 0.4, 0.5$ and $Re = 5$ and $Ma = 0.1$.

Fig. 7 displays the same information as Fig. 6 but for $Ma = 0.1$. Elastic energy is increased over the corresponding profiles for $Ma = 0.01$ while kinetic energy is slightly reduced. The increased compressibility produces a series of undershoots and overshoots in the evolution of kinetic energy. The number of overshoots and undershoots decreases and their magnitudes diminish with increasing We and have damped out for all cases by around $t = 4$ whereas for $Ma = 0.01$ they persist in time for $We = 0.5$.

Fig. 8 shows the influence of Ma on the evolution of the kinetic and elastic energy of the flow for $Re = 1$ and $We = 0.3$. As in the case for incompressible flow, the steady state kinetic energy of the fluid is reduced as the Weissenberg number is increased and stored elastic energy is significantly increased. Varying the Mach number in the range $0 \leq Ma \leq 0.1$ does not change the underlying behaviour. However, when the Mach number reaches 0.1 unstable behaviour in the flow persists for the first few seconds altering the kinetic energy profile (shown in Fig. 7).

The underlying qualitative behaviour of the flow is the same for both the compressible and incompressible cases. The Weissenberg number has a significant influence on the evolution of both kinetic and elastic energy. The kinetic energy grows as the lid accelerates, reaching a peak between $t = 0.5$ and $t = 1.5$ before falling to a steady state value. The elastic energy grows rapidly reaching a plateau proportional to the Weissenberg number. The Weissenberg number has little impact on the peak kinetic energy, which remains close to the steady state value for the Newtonian case. Compressibility does have a noticeable impact on the kinetic and elastic energy profiles. Increasing Ma increases the peak and steady-state kinetic energy and also increases the elastic energy.

Table 4

Compressible lid-driven cavity flow: Dependence of the minimum value of stream function and its location on Ma for $Re = 1$, $We = 0.5$.

Ma	ψ_{min}	x_{min}	y_{min}
0.001	−0.0643	0.4862	0.8124
0.01	−0.0599	0.4892	0.8266
0.1	−0.0532	0.4911	0.8353

As shown in Fig. 9(a) and (b) recirculation velocity weakens as We increases from 0 to 0.5. Fig. 9(a) tracks the x-component of the velocity field at the horizontal mid-point of the flow. Similarly Fig. 9(b) shows the y-component of the velocity along the line $[x, 0.75]$. Overall there is a net reduction in peak-velocity as We is increased which is demonstrated in the lower absolute maximum values in u_x and u_y in (a) and (b) for $We = 0.5$ compared to $We = 0.1$. Table 4 provides quantitative information about the influence of Ma on the minimum value of the stream function and its location.

For an inertia-less Newtonian fluid the recirculation vortex in the flow is symmetrical about the line $x = 0.5$. Elastic effects cause the symmetry to be broken. As the Weissenberg number is increased the location of the eye of the vortex moves progressively away from the centre in the opposite direction to the movement of the lid. This can be seen in Fig. 10 where the contours of the stream function are presented for $We = 0.1$ and $We = 0.5$ for $Re = 0$ and $Ma = 0.01$.

Contours of the three components of the steady-state viscoelastic extra-stress tensor are shown in Fig. 11 for $We = 0.5$, $\beta_v = 0.5$, $Re = 1$, $Ma = 0.01$. The stress component τ_{xx} has a boundary layer along the
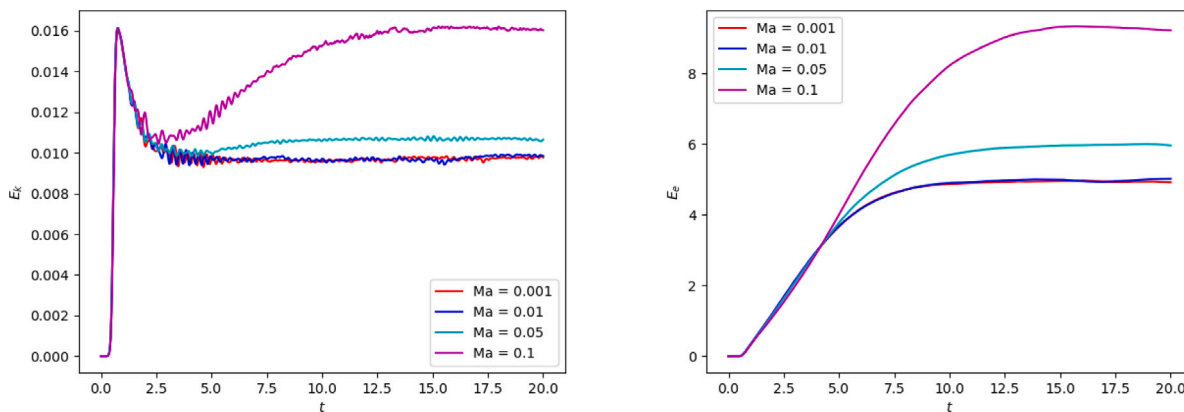
Fig. 8. Lid-driven cavity Flow: (a) kinetic and (b) elastic energy for $Ma = 0.001, 0.01, 0.1$, $Re = 1$ and $We = 0.5$.
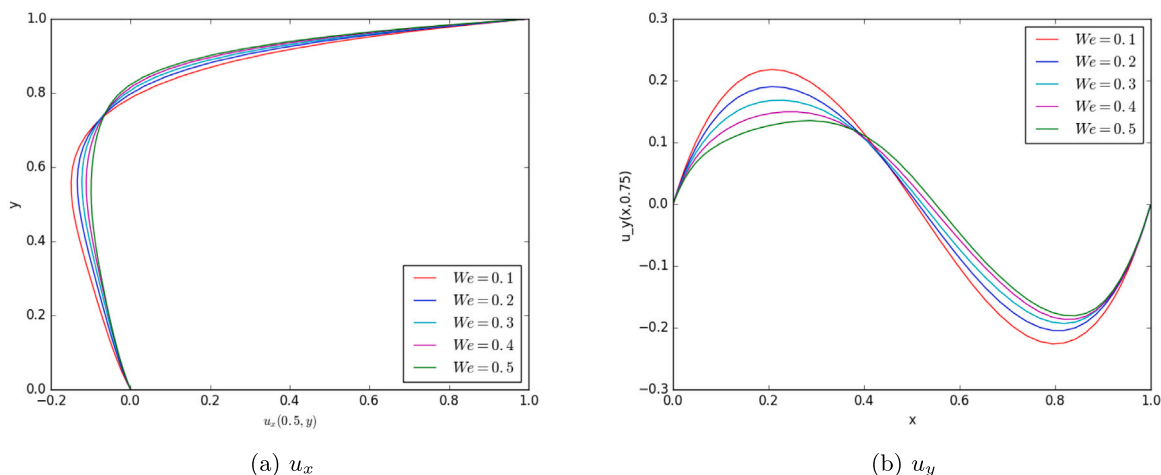

(a) u_x (b) u_y

Fig. 9. Lid-driven cavity Flow: Cross-section of velocity components for $We = 0.1, 0.2, 0.3, 0.4, 0.5$, and $Re = 1$ and $Ma = 0.01$.
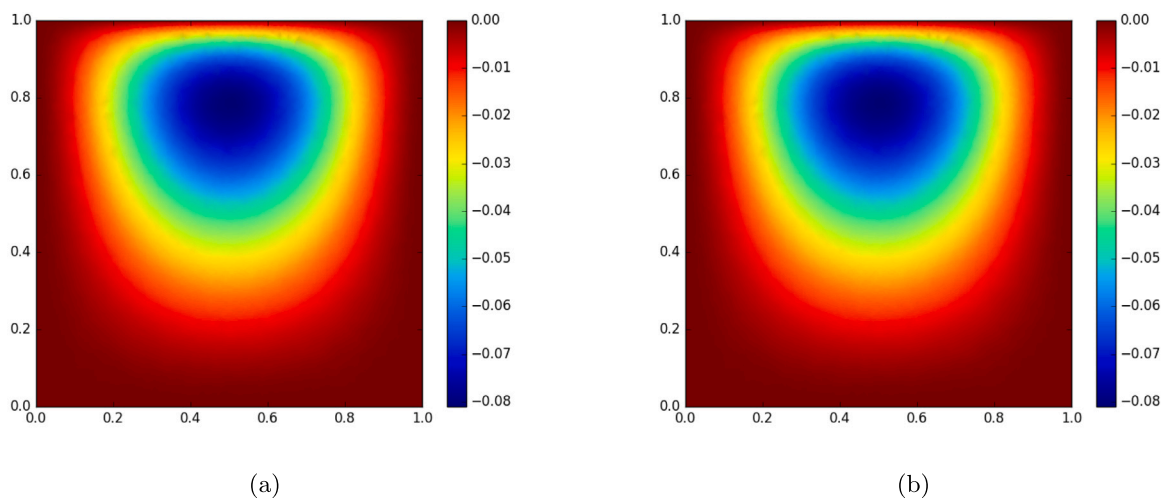

(a)   (b)

Fig. 10. Lid-driven cavity flow: contours of the stream function for (a) $We = 0.1$ and (b) $We = 0.5$ for $Re = 0$ and $Ma = 0.01$.

upper boundary whilst τ_{xy} and τ_{yy} display large gradients in the upper right-hand corner. The symmetry of the flow is broken due to elastic effects as a result of the asymmetry of the normal stress values. The eye of the recirculation region shifts upstream. However, this trend is weakened when the Reynolds number is increased above zero.

The kinetic energy is unaffected by changes in Ma and the elastic energy is decreased as Ma is increased meaning viscoelasticity and

compressibility have opposite effects on the elastic energy. However at low Mach numbers the results are close to those for incompressible flow.

The minimum value of the stream function is the measure used for quantitative comparisons with numerical investigations reported in the literature. For inertia-less Newtonian flow the eye of rotation remains in a central location. As the Weissenberg number increases the location
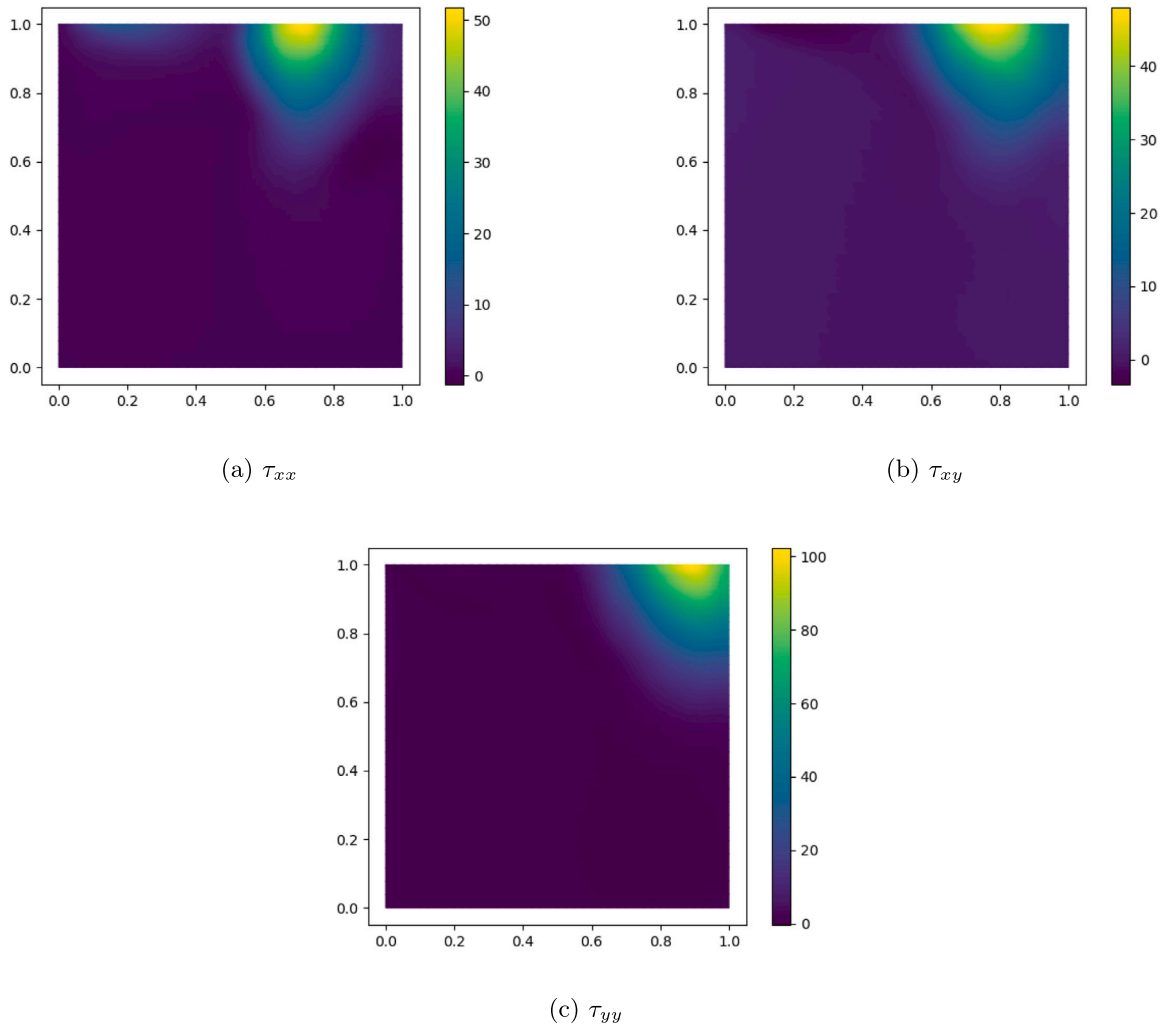
(a) τ_{xx}

(b) τ_{xy}

(c) τ_{yy}

Fig. 11. Lid driven cavity flow: contours of the stress components (a) τ_{xx}, (b) τ_{xy}, (c) τ_{yy} for $We = 0.5$, $\beta = 0.5$, $Re = 1$, $Ma = 0.01$.

Table 5
Compressible lid driven cavity flow: influence of the minimum value of the stream function, ψ_{min}, and its location on We and Ma for $Re = 0$ at $t = 15$.

	We				
Ma	0.1	0.25	0.5	0.75	1.0
0.001	−0.0813	−0.0718	−0.0643	−0.0482	−0.0425
	(0.4922,0.8255)	(0.4897,0.8206)	(0.4842,0.8123)	(0.4806,0.8116)	(0.4746,0.8095)
0.01	−0.0812	−0.0710	−0.0600	−0.0450	−0.0376
	(0.4927,0.8255)	(0.4902,0.8205)	(0.4862,0.8266)	(0.4816,0.8106)	(0.4760,0.8098)
0.1	−0.0811	−0.0695	−0.0532	–	–
	(0.4931,0.8265)	(0.4917,0.8228)	(0.4811,0.8353)	–	–

of the minimum value of the stream function shifts leftward and the symmetry of the flow is progressively broken. However, as the Reynolds number is increased, the eye of rotation shifts back towards the centre line $x = 0.5$. Increased compressibility also causes the eye of rotation to shift towards the centre line although the effect is relatively small at low Mach numbers.

Values of stream function minimum, ψ_{min}, and its location are tabulated in Tables 5–6. They provide insight into how steady-state flow characteristics are influenced by elasticity (We), inertia (Re) and compressibility (Ma). Table 5 compares the influence of We and Ma for $Re = 0$. When Ma is fixed, ψ_{min} increases with increasing We. Correspondingly the eye of the vortex moves slightly to the left but there are no major changes in its location for the range of parameters

considered. Table 6 compares the influence of Re and Ma for $We = 0.5$. For a fixed value of Ma, ψ_{min} increases slowly with increasing Re. Correspondingly the eye of the vortex moves slightly to the right with increasing Re but the change in its location is minimal for the range of parameters considered. Where there are missing values, a steady state solution was not attained.

7. Natural convection

In this section we consider the problem of buoyancy driven flow of an Oldroyd-B fluid in a square cavity whose vertical sides are kept at (different) constant temperatures and whose horizontal sides are partially insulated. More specifically, we impose the following boundary

Table 6

Compressible lid-driven cavity flow: influence of the minimum value of the stream function, ψ_{min}, and its location on Re and Ma for $We = 0.5$ at $t = 15$.

	Re				
Ma	1	5	10	25	50
0.001	−0.0643	−0.0623	−0.0592	−0.0581	−0.0574
	(0.4862,0.8124)	(0.4886,0.7866)	(0.4903,0.7686)	(0.4916,0.7458)	(0.4955,0.7215)
0.01	−0.0600	−0.0622	−0.0592	−0.0581	−0.0574
	(0.4892,0.8266)	(0.4905,0.7925)	(0.4915,0.7726)	(0.4918,0.7425)	(0.4925,0.7495)
0.1	−0.0532	−0.0530	−0.0527	–	–
	(0.4911,0.8353)	(0.4918,0.8236)	(0.4925,0.8056)	–	–

conditions on velocity and temperature

$$\mathbf{u}(t, x, 0) = \mathbf{u}(t, x, 1) = 0 = \mathbf{u}(t, 0, y) = \mathbf{u}(t, 1, y)$$

$$\theta(t, 0, y) = \theta_h(t), \quad \theta(t, 1, y) = 0,$$

$$\frac{\partial \theta}{\partial n}(t, x, 1) = Bi\theta, \quad \frac{\partial \theta}{\partial n}(t, x, 0) = 0 \tag{34}$$

where Bi is the Biot number defined by

$$Bi = \frac{Lh_c}{\kappa},$$

and

$$\theta_h(t) = \frac{1}{2}(1 + \tanh(8t - 4)).$$

The function $\theta_h(t)$ is chosen so that the temperature increases smoothly from a value near 0 to a value near 1.

The Boussinesq approximation, in which the thermophysical properties of the fluid are assumed to be constant (i.e. no equation of state coupling pressure, density and temperature) is invoked. This approximation replaces the body force term in the momentum equation in the governing Eqs. (1) with the term $RaPr\theta\mathbf{k}$. In this approximation the density is assumed to depend linearly on temperature and compressible effects are contained within the body force term using

$$\rho = \rho_0(1 - \beta(\theta - \theta_c)) \tag{35}$$

in the dimensional form of the equation where ρ_0 is the density at a reference temperature θ_c.

In the numerical simulations two quantities associated with the flow are reported. The first is the average Nusselt number defined by

$$\overline{Nu}(t) = \int_0^1 \frac{\partial \theta}{\partial n}(t, 0, y) \, dy, \tag{36}$$

which is a measure of overall heat transfer. An approximation of the normal derivative on the hot wall in Eq. (36) is made using the finite difference approximation

$$\frac{\partial \theta}{\partial n}(t, 0, y) \approx \frac{\theta(t, h_{0,y}, y) - \theta(t, 0, y)}{h_{0,y}}, \tag{37}$$

where $h_{0,y}$ is the length of the cell adjacent to the left-hand boundary in the x-direction, The second quantity is the steady-state maximum flow speed. These two quantities are calculated for different values of We and Ra keeping Pr and the other parameters fixed.

A structured mesh is used for this problem with increased mesh refinement near the cavity walls. In particular, we found that the most suitable choice of mesh was structured with a non-uniform distribution of finite elements clustered along the x-axis so that refinement occurs close to the left and right walls. The mesh is defined by

$$(x_i, y_j) = \left(\frac{1}{2} \left(1 - \cos \left(\frac{i\pi}{N} \right) \right), \frac{j}{N} \right), \quad 0 \le i, j \le N. \tag{38}$$

7.1. Incompressible flow

In this subsection we consider incompressible flow for which the Boussinesq approximation is used to describe the buoyancy forces. We begin by performing a mesh convergence study. Three finite element

Table 7

Natural convection flow: Characteristics of the finite element meshes M1–M3 for the buoyancy-driven flow problem.

Mesh	N	Cells	h_{min}	h_{max}	$DoF(p)$	$DoF(\mathbf{u})$	$DoF(C)$
M1	40	3200	0.02505	0.04652	1681	22722	19683
M2	60	7200	0.01668	0.03102	3721	50822	43923
M3	80	12800	0.01251	0.02327	6561	90242	77763

Table 8

Natural convection flow: Spatial and temporal convergence of the steady state value of $\overline{Nu}$ for $Ra = 1000$, $We = 0.1$ and $Pr = 1.0$, $\beta_v = 0.5$.

Δt	$M1$	$M2$	$M3$
0.005	0.824415	0.837543	0.848844
0.001	0.859169	0.860261	0.861656
0.0005	0.859504	0.860266	0.861697

Table 9

Natural convection flow: Steady-state values of E_k and $\overline{Nu}$ for meshes M1–M3 with flow parameters $Ra = 1000$, $We = 0.1$ and $Pr = 1.0$.

Mesh	E_k	$\overline{Nu}$
M1	0.460188	0.811989
M2	0.427991	0.823058
M3	0.413851	0.824643

meshes are considered, the characteristics of which are shown in Table 7. Spatial and temporal convergence data are provided in Table 8 and Fig. 12. The steady state Nusselt number, $\overline{Nu}$ converges up to two decimal places for meshes $M2$ and $M3$ when $\Delta t \le 0.001$. Fig. 12 shows the dependence of the evolution of the kinetic energy, E_k, and Nusselt number, $\overline{Nu}$, on mesh size for M1–M3. Converged approximations to these quantities are obtained on mesh M3 (see Table 9).

Table 10 shows the maximum flow speed attained for values of Ra and We in the range $10^2 \le Ra \le 10^4$ and $0 \le We \le 2$ for $Pr = 2$ and $\beta_v = 0.5$. The maximum flow speed increases rapidly with increasing Ra for each value of We considered. The introduction of viscoelasticity leads to an initial substantial decrease in the maximum flow speed as We is increased from $We = 0$ to $We = 0.1$ followed by a more gradual decrease as We is increased further to $We = 2$. A greater initial decrease in relative terms is observed with increasing Ra. For $We = 2$ the maximum flow speed has decreased to about 10% of its value at $We = 0$ for all values of Ra considered.

Table 11 presents the value of $\overline{Nu}$ over the same range of Ra and We for $Pr = 2$ and $\beta_v = 0.5$. Whilst the value of $\overline{Nu}$ increases with Ra, viscoelasticity works to counteract this effect in a powerful way. For example, at $Ra = 10^4$, $\overline{Nu} = 2.28$ for Newtonian flow ($We = 0$) which reduces to $\overline{Nu} = 1.10$ when $We = 2$. This is the same value obtained for Newtonian flow for $Ra = 10^2$. At high values of We there is weaker dependence of Ra on $\overline{Nu}$. For lower values of We, the influence of Ra on $\overline{Nu}$ is more significant with $\overline{Nu}$ increasing by almost a factor of two between $Ra = 10^2$ and $Ra = 10^4$ for $We = 0.1$. Increasing We has a larger impact on $\overline{Nu}$ for high values of Ra than for low values. Fig. 14 shows the effect on steady-state temperature of We at $Ra = 10^3$. These trends would suggest that elasticity has a negative effect on the capacity
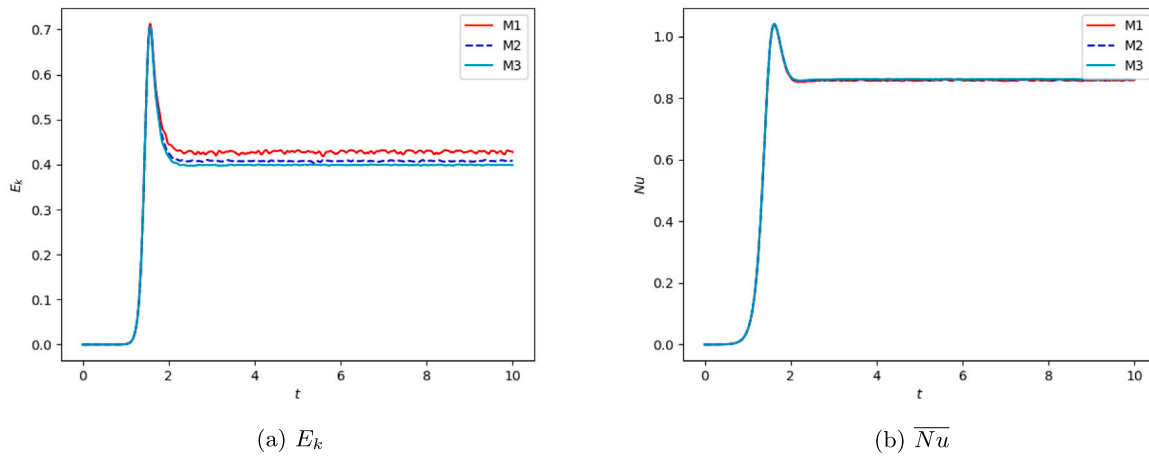
(a) E_k

(b) $\overline{Nu}$

Fig. 12. Natural convection flow: Influence of the evolution of (a) E_k, (b) $\overline{Nu}$ for meshes M1–M3 with flow parameters $Ra = 1000$, $We = 0.1$ and $Pr = 1.0$.

Table 10
Natural convection flow: dependence of the steady-state values of $\max|\mathbf{u}|$ on Ra and We, for $Pr = 2$, $\beta_v = 0.5$.

			Ra		
We	10^2	10^3	2×10^3	5×10^3	10^4
0	1.566	7.315	9.365	13.569	18.256
0.1	0.866	2.624	3.568	4.211	5.545
0.25	0.684	2.235	3.144	3.464	4.101
0.5	0.418	1.430	2.001	2.336	3.266
1.0	0.273	1.036	1.563	1.803	3.001
2.0	0.190	0.782	1.233	1.633	–

Table 11
Natural convection flow: dependence of the steady-state values of $\overline{Nu}$ on Ra and We, for $Pr = 2$, $\beta_v = 0.5$.

			Ra		
We	10^2	10^3	2×10^3	5×10^3	10^4
0	1.101	1.157	1.342	1.855	2.285
0.1	1.095	1.110	1.182	1.402	1.785
0.25	1.057	1.082	1.121	1.256	1.547
0.5	1.032	1.056	1.069	1.010	1.299
1.0	1.022	1.042	1.051	1.079	1.115
2.0	1.017	1.028	1.042	1.066	1.101

of a fluid to transfer heat via convection, especially for flows in the low Rayleigh number regime.

7.2. Weakly compressible flow

In order to fully couple the momentum and energy conservation laws we need to move beyond the Boussinesq approximation and use an equation of state relating density and temperature. Implicit in the weakly compressible Taylor–Galerkin scheme given in Section 5 is a relation between density and pressure of the form

$$p + B = B\rho^m \tag{39}$$

where B is a constant. This isothermal equation of state is derived empirically and is suitable for describing polymer melts and solutions and other liquids under the linear approximation ($m = 1$). In this case, the equation of state is

$$\frac{\partial p}{\partial \rho} = \frac{(B + p)m}{\rho} = c_0^2 \tag{40}$$

where c_0 is the speed of sound. A dimensionless nonisothermal extension to this equation is

$$\frac{\partial p}{\partial \rho} = \frac{1}{Ma^2}\left(\frac{1}{1 + \hat{\beta}\theta}\right) \tag{41}$$

where $\hat{\beta}$ is a thermal expansion coefficient. In the remainder of this paper we use $\hat{\beta} = 0.1$.

The Weissenberg number has a significant impact on the speed of the flow and, as a result, on the temperature distribution of the fluid during the transient phase and at steady state.

Fig. 13 and Fig. 14 show the effect on steady-state velocity magnitude and temperature of We at $Ra = 10^4$, respectively. These trends suggest that elasticity has a negative effect on the capacity of a fluid to transfer heat via convection, especially for flows at low-to-moderate Rayleigh numbers.

In Fig. 15 the evolution of the kinetic and elastic energies are presented for $Ra = 2 \times 10^3$ and $Ra = 5 \times 10^3$ and $Ma = 0.05$. In the range $0 < Ra \leq 5000$ the peak flow speed increases with Ra and We while the steady-state flow speed is adversely impacted by increasing We (Fig. 15(a)–(d)). However as Ra approaches 5000 this trend is reversed and it appears steady-state flow speed increases with both Ra and We (Fig. 15(e)–(f)). The impact of We on steady state flow speed has a noticeable effect on the temperature profiles and heat convection. Table 11 shows the value of $\overline{Nu}$ over the same range of Ra and We. Whilst $\overline{Nu}$ increases with Ra, the elasticity parameter counteracts this effect in a strong way. For example, at $Ra = 10^4$ $\overline{Nu} = 2.28$ for Newtonian flow ($We = 0$). This reduces to $\overline{Nu} = 1.1011$ when $We = 2.0$

8. Conclusions

The influence of compressibility, temperature and viscoelasticity on some benchmark problems in 2D is investigated using a new thermodynamically consistent model developed by Mackay and Phillips [41]. The new model circumvents the ad-hoc treatment of temperature that pervades many contributions in the literature. Fluids are characterised using a small number of dimensionless groups which enables the combined and separate effects of compressibility, temperature and viscoelasticity on flow characteristics to be evaluated.

The dimensionless governing equations for this new thermodynamically consistent model are discretised using a stabilised Taylor–Galerkin finite element method. The temporal scheme is based on a second-order Taylor–Galerkin pressure-correction scheme and within each time step Galerkin finite elements are used for the spatial discretisation. Enhanced numerical stability is achieved through use of the DEVSS formulation which has been modified for use in compressible flows. This formulation increases the ellipticity of the momentum equation. A local projection stabilisation scheme is used to overcome the instabilities in the discretisation of the constitutive equation caused by the so-called high Weissenberg number problem. The use of these stabilisation techniques for this class of flows represents an original contribution of this paper.
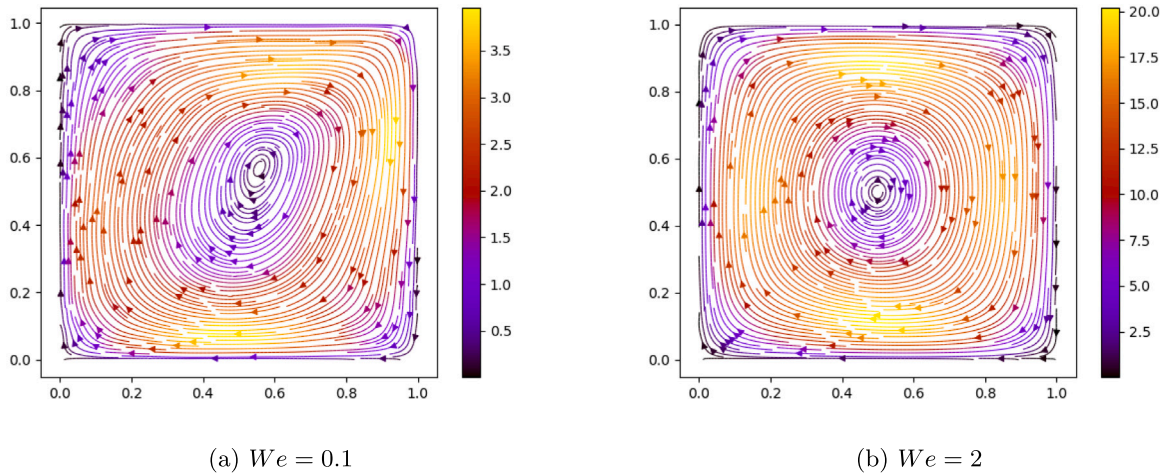
(a) $We = 0.1$

(b) $We = 2$

Fig. 13. Natural convection flow: contours of the magnitude of the steady-state velocity for (a) $We = 0.1$ and (b) $We = 2$ and $Ra = 1 \times 10^4$.

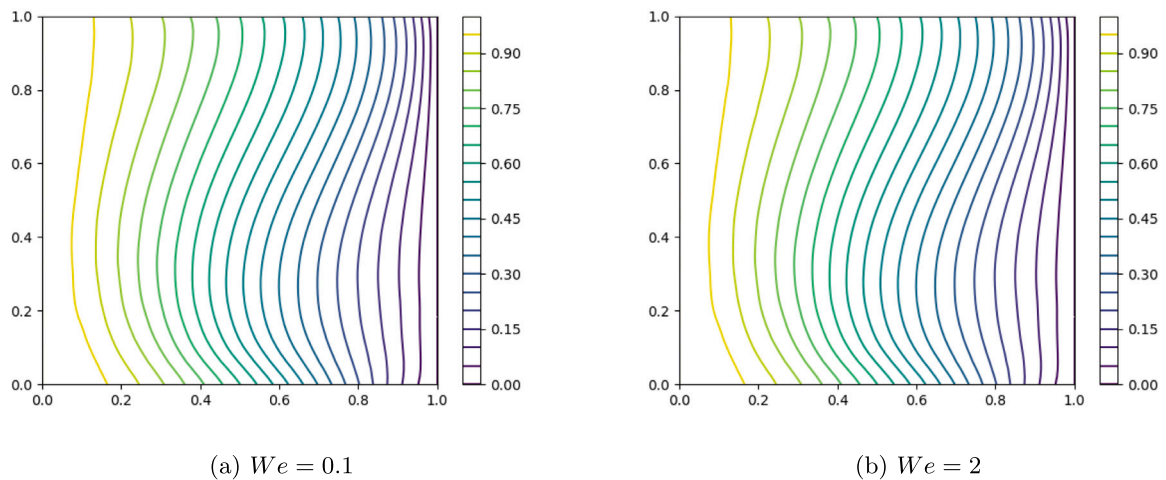(a) $We = 0.1$

(b) $We = 2$

Fig. 14. Natural convection flow: contours of the steady-state temperature for (a) $We = 0.1$ and (b) $We = 2.0$ and $Ra = 1 \times 10^4$.

Two benchmark problems in square domains are considered. These represent the first application of the stabilised scheme described in this paper to the variant of these benchmark problems that include compressible and nonisothermal considerations. The first benchmark problem considered was the lid-driven cavity problem. The minimum value of the stream function, ψ_{min}, is one of the flow characteristics that is used as a basis of comparison of numerical methods for incompressible flow. Good agreement is obtained with the literature [1,31] demonstrating that the alternative formulation yields reliable results as $Ma \to 0$. The numerical scheme demonstrated good stability characteristics for $0.001 < Ma < 0.1$ and results for very low Mach numbers were close to the incompressible predictions as expected. Compressibility has the effect of reducing the magnitude of ψ_{min}, but otherwise does not have a significant impact on the qualitative behaviour of the flow. Kinetic energy is largely unaffected by changes in Ma. The most significant changes occur in the elastic energy where compressibility and viscoelasticity have opposite effects. For a fixed value of Ma, elastic energy increases with increasing We, whereas for a fixed value of We, it decreases with increasing Ma. Quantitatively, for $We = 0.5$ there is a 50% reduction in the steady state elastic energy when Ma is increased from 0.001 to 0.1 whereas for $Ma = 0.1$ there is an almost order of magnitude increase in the steady state elastic energy when We is increased from 0.1 to 0.5. Future work will focus on obtaining

numerically stable solutions for a larger range of Mach and Weissenberg numbers (i.e. $Ma > 0.1$ and $We > 2.0$).

The second benchmark problem considered was natural convection in a cavity. The usual Boussinesq approximation was not adopted and incompressibility was not imposed which enabled the effects of density and gravity to be studied using an equation of state. The stabilised Taylor–Galerkin finite element scheme enabled stable numerical approximations to be obtained for a range of Ma, Ra and Pr. The numerical model predicted a reduction in kinetic energy with increasing We which implies, at least intuitively, that viscoelastic fluids exhibit a potential for increasing the critical Rayleigh number of the flow. For all values of Ra, the average Nusselt number decreases with increasing values of We with the most dramatic decreases occurring for the largest values of Ra considered. Thus, for the range of parameters considered in this paper, viscoelasticity reduces the overall heat transfer in the convection cell.

In this paper we have focussed on incorporating additional capabilities into the computational model and investigating the stabilisation of the traditional formulation of the constitutive equation. Although the log-conformation approach has been shown to stabilise the numerical simulation of incompressible isothermal viscoelastic flows, its extension to constitutive equations for compressible viscoelastic fluids in which
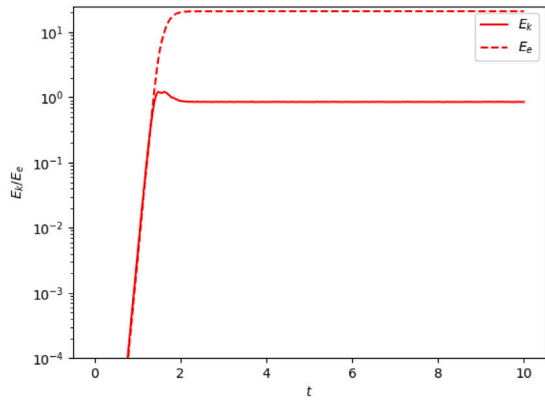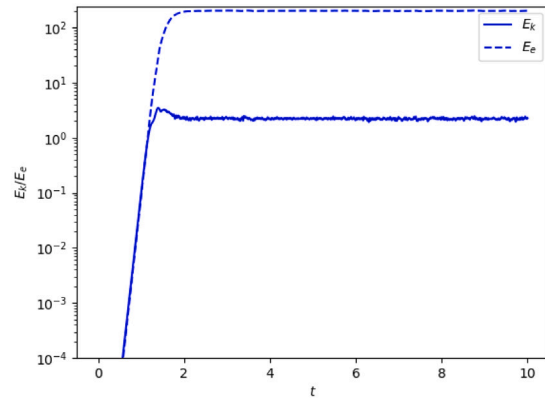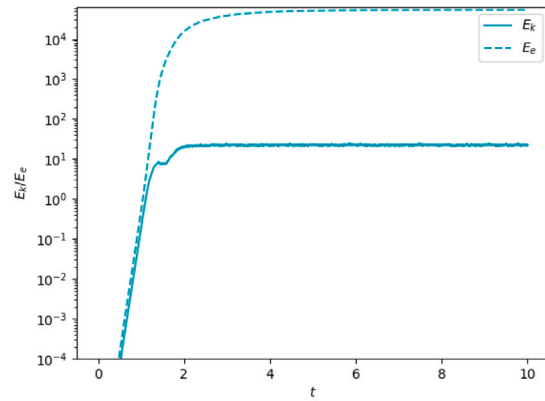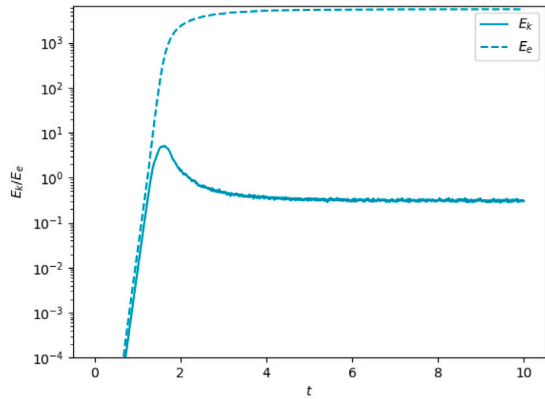
(a) $Ra = 2 \times 10^3$, $We = 0.1$ (b) $Ra = 1 \times 10^4$, $We = 0.1$
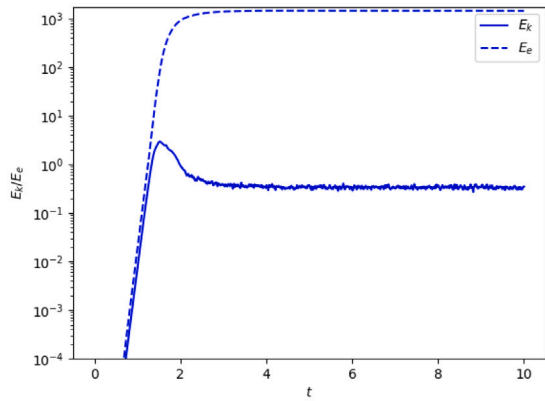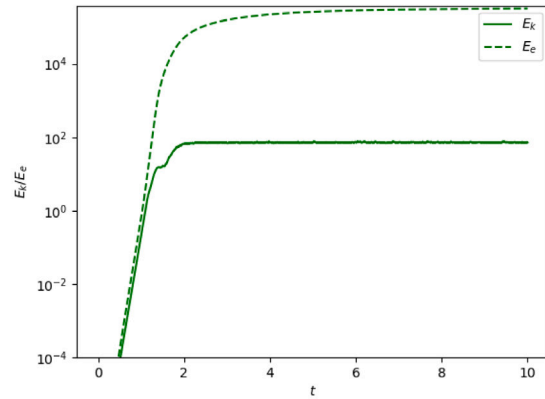
(c) $Ra = 2 \times 10^3$, $We = 1.0$ (d) $Ra = 1 \times 10^4$, $We = 1.0$

(e) $Ra = 2 \times 10^3$, $We = 2.0$ (f) $Ra = 1 \times 10^4$, $We = 2.0$

Fig. 15. Natural convection flow: evolution of the kinetic and elastic energy for $We = 0.1, 1, 2$, $Ra = 2 \times 10^3, 1 \times 10^4$ and $Ma = 0.05$.

the material parameters are replaced by temperature dependent material functions has not been established. This is an interesting research question and one which we wish to explore in future work.

CRediT authorship contribution statement

A.T. Mackay: Conceptualization, Methodology, Software, Visualization, Investigation, Data curation, Writing – original draft, Writing – review & editing. **T.N. Phillips:** Conceptualization, Methodology, Writing – original draft, Writing – review & editing, Project administration.

Declaration of competing interest

The authors declare that they have no known competing financial interests or personal relationships that could have appeared to influence the work reported in this paper.

Data availability

Data will be made available on request.

Acknowledgements

References

[1] Venkatesan J, Ganesan S. A three-field local projection stabilized formulation for computations of Oldroyd-B viscoelastic fluid flows. J Non-Newton Fluid Mech 2017;247:90–106.

[2] Bollada PC, Phillips TN. On the mathematical modelling of a compressible viscoelastic fluid. Arch Ration Mech An 2012;205(1):1–26.

[3] Keshtiban IJ, Belblidia F, Webster MF. Compressible flow solvers for low Mach number flows—a review. Internat J Numer Methods Fluids 2004;23:77–103.

[4] Beris AN. Thermodynamics of flowing systems: with internal microstructure. New York: Oxford University Press; 1994.

[5] Edwards BJ, Beris AN. Unified view of transport phenomena based on the generalized bracket formulation. Ind Eng Chem Res 1991;30(5):873–81.

[6] Brooks AN, Hughes TJ. Streamline upwind/Petrov-Galerkin formulations for convection dominated flows with particular emphasis on the incompressible Navier-Stokes equations. Comput Method Appl M 1982;32(1–3):199–259.

[7] Marchal JM, Crochet MJ. A new mixed finite element for calculating viscoelastic flow. J Non-Newton Fluid Mech 1987;26(1):77–114.

[8] Guénette R, Fortin M. A new mixed finite element method for computing viscoelastic flows. J Non-Newton Fluid Mech 1995;60(1):27–52.

[9] Rajagopalan D, Armstrong RC, Brown RA. Finite element methdos for calculation of steady, viscoelastic flow using constitutive equations with a Newtonian viscosity. J Non-Newton Fluid Mech 1990;36:159–92.

[10] Brown RA, Szady MJ, Northey PJ, Armstrong RC. On the numerical stability of mixed finite-element methods for viscoelastic flows governed by differential constitutive equations. Theor Comput Fluid Dyn 1993;5(2):77–106.

[11] Fortin M, Fortin A. A new approach for the FEM simulation of viscoelastic flows. J Non-Newton Fluid Mech 1989;32(3):295–310.

[12] Balci N, Thomases B, Renardy M, Doering CR. Symmetric factorization of the conformation tensor in viscoelastic fluid models. J Non-Newton Fluid Mech 2011;166(11):546–53.

[13] Afonso A, Pinho F, Alves M. The kernel-conformation constitutive laws. J Non-Newton Fluid Mech 2012;167:30–7.

[14] Saramito P. Efficient simulation of nonlinear viscoelastic fluid flows, vol. 60, 1995, p. 199–223.

[15] Castillo E, Codina R. First, second and third order fractional step methods for the three-field viscoelastic flow problem. J Comput Phys 2015;296:113–37.

[16] Pacheco DRQ, Castillo E. Consistent splitting schemes for incompressible viscoelastic flow problems. Internat J Numer Methods Engrg 2023;124(8):1908–27.

[17] Webster MF, Keshtiban IJ, Belblidia F. Computation of weakly-compressible highly-viscous liquid flows. Eng Comput 2004;21(7):777–804.

[18] Numerical simulation of compressible viscoelastic liquids. J Non-Newton Fluid Mech 2004;122(1):131–46.

[19] Ostrach S. Natural convection in enclosures. J Heat Transf 1988;110(4-B):1175–90.

[20] Sparrow E, Eichhorn R, Gregg J. Combined forced and free convection in a boundary layer flow. Phys Fluids 1959;2(3):319–28.

[21] Batchelor G. Heat transfer by free convection across a closed cavity between vertical boundaries at different temperatures. Quart Appl Math 1954;12(3):209–33.

[22] Ostrach S. Laminar flows with body forces. In: Moore FK, editor. Theory of laminar flows. Princeton, New Jersey: Princeton University Press; 1964, p. 528–718.

[23] Ostrach S. Completely confined natural convection. In: Proceedings of 10th midwestern mechanics conference. Colorado State University; 1967.

[24] Kim GB, Hyun JM, Kwak HS. Transient buoyant convection of a power-law non-Newtonian fluid in an enclosure. Int J Heat Mass Trans 2003;46(19):3605–17.

[25] Pittman J, Richardson J, Sherrard C. An experimental study of heat transfer by laminar natural convection between an electrically-heated vertical plate and both Newtonian and non-Newtonian fluids. Int J Heat Mass Trans 1999;42(4):657–71.

[26] Perera MGN, Walters K. Long-range memory effects in flows involving abrupt changes in geometry: Part I: flows associated with I-shaped and T-shaped geometries. J Non-Newton Fluid Mech 1977;2:49–81.

[27] Mendelson MA, Yeh PW, Brown RA, Armstrong RC. Approximation error in finite element calculation of viscoelastic fluid flows. J Non-Newton Fluid Mech 1982;10:31–54.

[28] Mackay AT, Phillips TN. Compressible and nonisothermal viscoelastic flow between eccentrically rotating cylinders. Theor Comput Fluid Dyn 2021;35(5):731–56.

[29] Brown RA, Szady MJ, Northey PJ, Armstrong RC. On the numerical stability of mixed finite-element methods for viscoelastic flows governed by differential constitutive equations. Theor Comput Fluid Dyn 1993;5:77–106.

[30] Liu AW, Bornside D, Armstrong R, Brown R. Viscoelastic flow of polymer solutions around a periodic, linear array of cylinders: Comparisons of predictions for microstructures and flow fields. J Non-Newton Fluid Mech 1998;77:153—190.

[31] Castillo E, Codina R. Numerical analysis of a stabilized finite element approximation for the three-field linearized viscoelastic fluid problem using arbitrary interpolations. ESAIM-Math Model Num 2017;51(4):1407–27.

[32] Barrenechea GR, Castillo E, Codina R. Time-dependent semidiscrete analysis of the viscoelastic fluid flow problem using a variational multiscale stabilized formulation. IMA J Numer Anal 2019;39:792–819.

[33] Ganesan S, Matthies G, Tobiska L. Local projection stabilization of equal order interpolation applied to the Stokes problem. Math Comp 2008;77(264):2039–60.

[34] Owens RG, Phillips TN. Computational rheology. 2nd ed.. London: World Scientific; 2002.

[35] Sousa R, Poole R, Afonso A, Pinho F, Oliveira P, Morozov A, et al. Lid-driven cavity flow of viscoelastic liquids. J Non-Newton Fluid Mech 2016;234:129–38.

[36] Logg A, Mardal K-A, Wells G. Automated solution of differential equations by the finite element method: the fEniCS book, vol. 84, Springer Science & Business Media; 2012.

[37] Mackay AT. 2020. https://github.com/ATMackay/fenics.

[38] Fattal R, Kupferman R. Time-dependent simulation of viscoelastic flows at high weissenberg number using the log-conformation representation. J Non-Newton Fluid Mech 2005;126(1):23–37.

[39] Pan T-W, Hao J, Glowinski R. On the simulation of a time-dependent cavity flow of an Oldroyd-B fluid. Internat J Numer Methods Fluids 2009;60(7):791–808.

[40] Xu S, Davies AR, Phillips TN. Pseudospectral method for transient viscoelastic flow in an axisymmetric channel. Numer Methods Partial Differential Equations 1993;9(6):691–710.

[41] Mackay AT, Phillips TN. On the derivation of macroscopic models for compressible viscoelastic fluids using the generalized bracket framework. J Non-Newton Fluid Mech 2019;266:59–71.